FERROMAGNETIC Fe-Cu COATING FOR FERROUS CONTAMINANTS

SENSING IN AQUEOUS MEDIA

by

Abdullah Abou Hewelle

A Thesis presented to the Faculty of the
American University of Sharjah
College of Engineering
In Partial Fulfillment
of the Requirements
for the Degree of

Master of Science in
Mechanical Engineering

Sharjah, United Arab Emirates

November 2020

Declaration of Authorship

I declare that this thesis is my own work and, to the best of my knowledge and belief, it does not contain material published or written by a third party, except where permission has been obtained and/or appropriately cited through full and accurate referencing.

Signed   Abdullah Abou hewelle

Date   19/11/2020

Approval Signatures

We, the undersigned, approve the Master's Thesis of Abdullah Abou Hewelle

Thesis Title: Ferromagnetic Fe-Cu Coating for Ferrous Contaminants Sensing in

Aqueous Media.

Date of Defense: 26/11/2020

Name, Title and Affiliation	Signature

_____

Dr. Mehdi Ghommem
Associate Professor, Department of Mechanical Engineering
Thesis Advisor

_____

Dr. Abdul Hai Al Alami
Associate Professor, Department of Sustainable and
Renewable Energy Engineering
University of Sharjah
Thesis Co-Advisor

_____

Dr. Maen Alkhader
Associate Professor, Department of Mechanical Engineering
Thesis Committee Member

_____

Dr. Rana Sabouni
Associate Professor, Department of Chemical Engineering
Thesis Committee Member

_____

Dr. Mamoun F. Abdel-Hafez
Head
Department of Mechanical Engineering

_____

Dr. Lotfi Romdhane
Associate Dean for Graduate Studies and Research
College of Engineering

_____

Dr. Sirin Tekinay
Dean
College of Engineering

_____

Dr. Mohamed El-Tarhuni
Vice Provost for Graduate Studies
Office of Graduate Studies

Acknowledgement

I would like to thank my advisors Dr. Mehdi Ghommem and Dr. Abdul Hai Al Alami for providing knowledge, guidance, support, and motivation throughout my research stages. I am deeply beholden for their great assistance, worthy discussion, and suggestions.

I would like to thank the professors of the Mechanical Engineering department who taught me the master level courses with mighty teaching methods and skills. I really appreciate their dignified advices and motivation.

Finally, I would like to thank the American University of Sharjah for the opportunity given to me as a Graduate Teaching Assistant, and the financial support via the AUS research grant (EN6001). I would also like to acknowledge the assistance of the University of Sharjah's supporting facilities including the Advanced Materials Research Laboratory.

Dedication

To my family, friends and everyone who supported me during this journey.

Abstract

This work investigates the development and analysis of a novel resonant sensor for ferrous contaminations in aqueous media. Resonant sensor is a class of sensors that employ a structure vibrating at resonance. Hence, the proposed sensing device works on the principle of detecting the dynamic response of a vibrating beam resulting from the attraction of iron contaminants present in aqueous solutions to its surface. The ferromagnetic property of the Fe-Cu bimetallic alloy is utilized to capture the contaminants as it is applied as a coating layer on aluminium components. The synthesis of the ferromagnetic material and the coating process were carried out in a planetary ball mill which allows the formation of a homogenous coating layer at low operating temperatures. Microstructural characterization tests, including XRD, SEM and EDS, were performed to confirm the formation of the single-phase Fe-Cu alloy and inspect the structural features of the coating layer. A series of experiments was conducted to examine the quality of the deposition of the coating material and select the optimum synthesis process parameters. Experimental results revealed a successful deposition of a 499 nm thickness layer of the Fe-Cu alloy on the aluminum substrate after coating for 5 hours at a rotational speed of 600 rpm. The produced coated beam samples have the ability of carrying a maximum of 7 mg of iron powder. An experimental set-up, comprising a mini shaker, a laser distance sensor, and a function generator, was built and used to investigate the proposed sensing mechanisms and validate the developed mathematical continuous model for beams fully immersed in fluid media subject to base excitation. This model was also used to generate the frequency responses of the coated beam in different fluid media and predict the change in its dynamic response resulting from the added mass when exposed to iron contaminants in water showing a 0.1 Hz shift in natural frequency due to added mass equivalent to 2% of the mass of the beam.

Keywords: *Fe-Cu alloy, ferrous contaminants, vibrating beam, resonant sensor, frequency response.*

Table of Contents

List of Figures

List of Tables

List of Abbreviations and Symbols

Ω_e	excitation frequency
A_m	added mass coefficient
c_h	hydraulic damping coefficients
c_s	structural damping coefficients
f_v	natural frequency of the beam in vacuum
m_0	mass
m_f	total mass of the coating material and ferrous contaminants
ξ_h	hydraulic damping ratio
ξ_s	structural damping ratio
ρ_f	density of the fluid
Δm	added mass
BCC	Body Centered Cube
EDS	Energy Dispersive X-Ray
FCC	Face Centered Cube
LOD	Limit of detection
MEMS	Micro-electromechanical systems
MOF	Metal Organic Framework
SEM	Scan Electron Microscope
XRD	X-Ray Diffraction
ω	natural frequency
E	Young's modulus
I	second moment of area

Y	excitation amplitude
f	natural frequency of the vibrating beam in a fluidic domain
j	unit imaginary number.
k	stiffness
$q(t)$	modal coordinate
β	mode number
μ	viscosity
ν	Poisson's ratio
ξ	total damping ratio
ρ	density
$\varphi(x)$	mass-normalized mode shape

Chapter 1. Introduction

In this chapter, an overview about the existence of iron contamination in water bodies and underground water around the globe is presented. Its allowable limit is stated and the serious consequences on human health when exceeding this limit are highlighted. Then, the main objective of this work is described stating the problem and summarizing the approach followed to solve this issue. Finally, the research contribution and the general organization of the Thesis are presented.

1.1. Overview

Iron constitutes one of the naturally existing metal ions in earth crust and soil, water bodies and underground water. The highest permissible amount of iron in drinking water, as specified by the World Health organization is 0.3 mg/l [1]. The existence of heavy iron contaminations in rivers and groundwater has been observed in many areas including Upper Yamuna [2], Swarnamukhi [3], and Burdwan [4]. A study by Borah et al. [5] reported on 11 samples out of 25 exceeding the permissible amount of iron in drinking water in Darrang district, Assam, India. Moreover, Figure 1 shows a mapping of areas in USA with iron limits below and exceeding the 0.3mg/L limit [6]. This figure reveals the significant presence of iron in US groundwater.
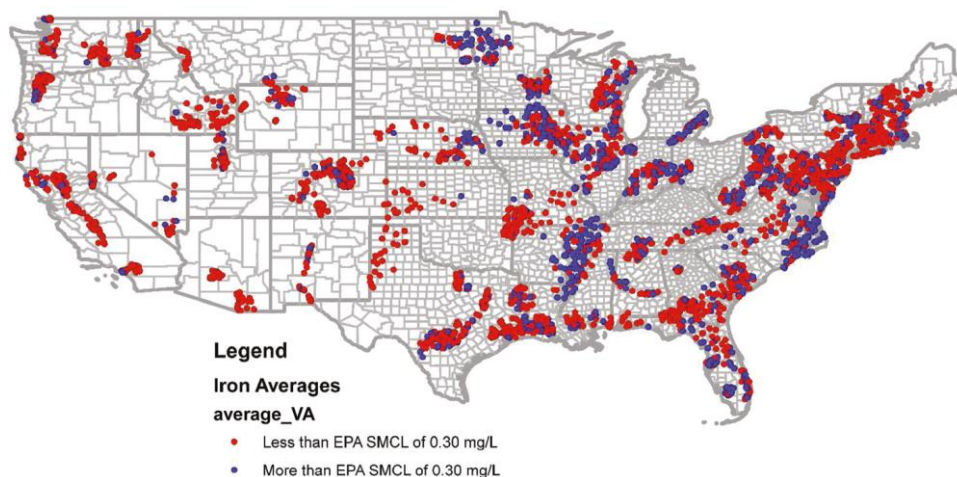

Figure 1 Average concentration of iron in U.S. groundwaters for the years 1990-2010 [6].

An extensive amount of iron intake may lead to iron overload which is directly related to several serious diseases such as Thalassemia, Hemochromatosis, diabetes mellitus, chronic liver disease, arthritis Parkinson, heart failure, Alzheimer, and some

13

kinds of cancers [7] [8]. In a study dealing with the effect of contaminated drinking water on human health in Dakahlyia Governorate, Egypt, the goal was to relate certain contaminants in drinking water to common and recurring diseases in that area [9]. It was found that liver cirrhosis cases were related to iron-contaminated drinking water. Trace elements were studied using atomic absorption spectrophotometer (AAS) [9]. Wen et al. [10] showed in their 11 years study conducted on 309443 adults in Taiwan that 35% of the males and 18% of the females of their sample showed a high serum iron level ($>120\mu/dL$) which was related to higher risk of liver and breast cancer [10]. Moreover, it is worth mentioning that a study by Mirlohi et al. [6] showed that people aged above 50 cannot sense iron in water by taste until it exceeds an average of 0.498 mg/L.

Laboratory procedures exist to detect and quantify the iron content. These procedures include but are not limited to atomic spectrometry, spectrophotometry, chemiluminescence, and voltammetry in addition to chromogenic method [11] [12]. However, they require the use of sophisticated equipment, the collection of samples from aquatic environments on a regular basis, or the deployment of expensive solvents and reagents, and a long lead time for sample treatment and analysis in the cases of fluorescence and colorimetry [13]. As such, there is need for the development of an efficient, highly sensitive and reliable detection and sensing devices for iron in aquatic environment that can perform real-time monitoring of water contamination based on on-site measurements of iron concentrations. This technology will allow environmental protection agencies to actively detect and counteract iron pollution before it can spread and harm human's health.

1.2.   Thesis Objectives

In this work, a novel material for detecting ferrous contaminants that can be used in a miniature sensing device is presented. This device utilizes the ferromagnetic property of the Fe-Cu metastable alloy layer coated on a cantilever beam shaped substrate. The idea is to use the change in the static and dynamic response of a vibrating beam resulting from the attraction of iron particles/ions by the coating material to detect the presence of iron and estimate its concentration. As a proof of concept, aluminum samples are coated, characterized, and tested for the purpose of this sensing application. The coating method relies on a simple sustainable coating technique utilizing the kinetic

energy of the particles moving inside a planetary ball mill. A set of characterization tests including XRD, SEM and EDS have been conducted to inspect the quality of the developed coating material. Moreover, an experimental set-up, comprising a mini shaker, laser distance sensor, and function generator, is implemented to examine the operability of the sensing system, assess its performance and reliability, and investigate two detection mechanisms: static and dynamic modes. Finally, a mathematical model of the design is formulated to simulate the dynamic behavior of the device and generate the frequency response of the coated Aluminum beam immersed in contaminated water.

1.3. Research Contribution

The following points highlight the significance of the present work:

- Present a thorough literature study about iron contamination in water and its effects on the human health, and the most well-established methods of detecting iron contaminations in aqueous solutions including Fluorescence, Colorimetric, MEMS and Metal Organic Framework sensors.
- Experimentally study the Ball Milling technique as an efficient method of synthesizing and coating the Fe-Cu binary alloy on substrates and analysing the outputs to tune the process parameters and enable better control of the outcomes.
- Explore the ferromagnetic behaviour of the Fe-Cu alloy and quantify its magnetic strength using a creative approach.
- Propose a cost-effective miniature Ferrous contaminants resonant sensor that exploits the ferromagnetic properties of the Fe-Cu coating layer and the sensitivity of the dynamic and static responses of vibrating beams to added mass.
- Conduct experimental and numerical analyses of the sensing mechanisms.

1.4. Thesis Organization

The next parts of this work are organized as follows: Chapter 2 provides a thorough literature review of the previous works on the detection of iron contaminations in aqueous solutions, an overview on the use of the ball milling technique and the Fe-Cu alloy properties. Moreover, a theoretical background is presented discussing a mathematical model of the proposed resonant sensor. Chapter 3 presents the experimental methodology along with the microstructural characterization techniques. The proposed experimental setup is illustrated and explained in Chapter 4. The results

and the main outcomes of this study are presented and discussed in Chapter 5. Finally, Chapter 6 presents the concluding remarks and the future work that can be done to further enhance this work.

Chapter 2. Literature Review and Theoretical Background

2.1   Literature Review

The serious risks of the excessive iron contaminants in water supply have prompted various research efforts aiming to explore and develop iron detection techniques and sensors. Sahu et al. [14] reported in their study on surfactant-free copper nanoclusters as a fluorescence biosensor sensor utilized to detect iron (III) in aqueous solutions and biomolecules with limit of detection (LOD) of 2µM and 0.8µM, respectively [14]. Polymer dots were reported by Chan et al. as a sensor capable of detecting Cu^{2+} and Fe^{2+} by methods of fluorescent probe [15]. Another study by Li et al. presented a modified silver nanoparticles (4-MBA-TMB-AgNP) sensor that operates based on the principle of colorimetry where the solution changes color from gray-white to purple when sensing iron (II) with a detection limit of 1.00 µM [16]. Kumar et al. [17] presented a colorimetric strip sensor that detects iron in aqueous solutions after 15 minutes interaction between the sensor and the solution where the minimal concentration detectable by naked eye was found equal to 50 ng/mL [17]. Moreover, Zhang et al. [13] conducted an experimental investigation on the dual response of fluorescent probe with the capability to detect iron and copper ions with a LOD of 0.12µM and 0.14 µM , respectivly [13]. Another photoluminescent sensor was proposed and developed by Mahmoud et al. [18]. It demonstrated high selectivity of iron in aqueous solutions and a detection limit of 1.56 x 10^{-5} mol/L [18].

The sensing of iron contaminants by employing metal-organic framework (MOF) materials constitutes one of the rapidly growing routes, given their outstanding characteristics, such as high specific surface areas and tunable pore size, and easy functionalization of the organic part upon selection of different metal ions and organic bridging ligands [19]. Wang et al. [20] reported on a nanoscale MOF colorimetric sensor cable of detecting Fe^{3+} with a color changing effect noticeable to the naked eye. Moreover, highly sensitive MOF fluorescent sensor was developed by Hu et al. [21] that is capable of detecting iron cation with a quenching constant of 2.893 x 10^4 M^{-1}. Another multifunctional luminescent MOF sensor was developed by Guo et al. [22] with the capability of detecting iron ions with an LOD of 0.39 µM. Finally, in some studies MOFs were used not only as a sensing method but also as a treatment technique of arsenic water, with adsorption capacity up to 115 mg/g iron [23].
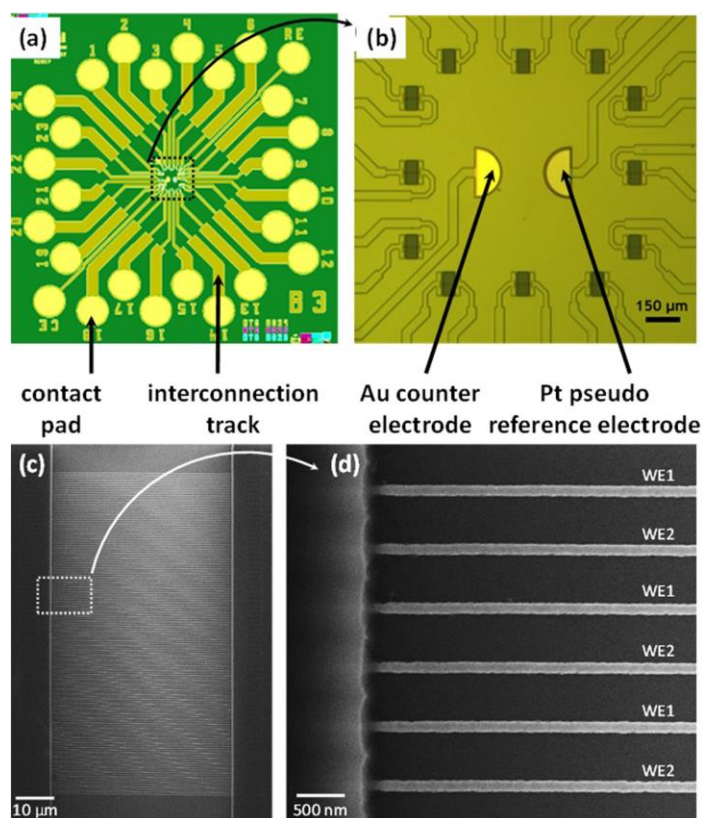
Figure 2. (a)Schematic, (b)Micrograph, (c) and (d) SEM images showing the iron sensing device suggested by Wahl et al [24].

As the discussion of material selection for sensor composition continues, the integration of such material into a suitable sensing device deserves no less attention. Wahl et al. [24] proposed a device of interdigitated nanowire electrode arrays used for the detection of iron shown in Figure 2. The device dimensions are 100 nm in width,50 nm in height, ~45 µm long and with 500 nm spacing placed on a Si/SiO_2. The LOD was found in the order of 0.6 mg/L [24]. Over the last two decades, the use of micro-electro-mechanical systems (MEMS) sensors has received significant attention by the scientific community in areas such as mass, chemical and bio-molecules detection. A study by Wang et al. [25] proposed a bio-inspired miniaturized sensor for lead detection showing sensitivity of 32 nA/(µg/L) with a detection time of 30s [25]. Another work by Possas-Abreu et al. [26] showed a successful design and implementation of a MEMS sensor capable of detecting 12 organic compounds in vapor. Moreover, Khan et al. [27]

reported on the design of a sensor detecting mycobacterium tuberculosis utilizing a MEMS cantilever beam capable of detecting the bacteria in patient's blood.

One of the technologies being utilized to make MEMS devices oriented towards a certain application is the coating on the surface of a vibrating microstructure. For example, Jaber et al. [28] deployed a Metal Organic Framework coating on an electrically actuated microbeam to develop a miniature sensor for simultaneous detection of water vapor and temperature. Holthoff et al. [29] proposed the use of molecularly imprinted polymers for identifying elements in MEMS chemical sensors. In addition, Pandya et al. [30] were able to coat a microstructure with functionalized layer with the purpose to diagnose breast cancer.

There are several routes for introducing the material with an affinity to a target analyte or contaminant to the surface of the sensing element. Some of these routes are chemical (e.g. CVD), physical (sputtering) or mechanical. Mechanical depiction technologies are usually selected due to their reliability, cost-effectiveness and being dry technologies that need not chemicals or extreme operating conditions (high temperature or pressure). Planetary ball mills work on the simple principle of the rotation of a sun and planet disks as illustrated in Figure 3. This technique is commonly used in the synthesis of alloys that are naturally immiscible or difficult to produce via conventional alloying techniques. It utilizes the kinetic energy of the moving balls to make the alloying process occur rather than suppling thermal energy to heat the alloy components [31] [32].
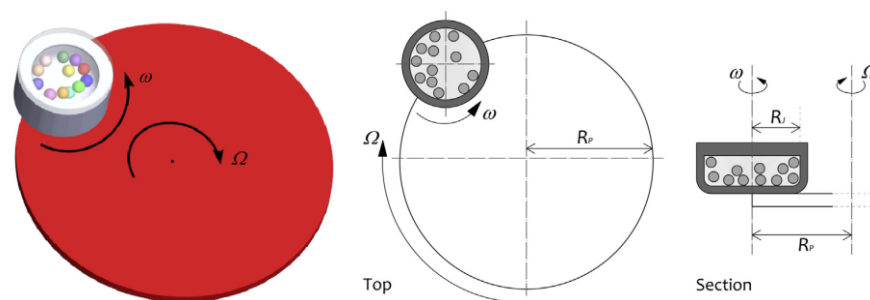

Figure 3 Schematic of the motion of planetary ball mills [31].

There are several studies that attempted to exploit the concept of the ball milling process that produces high levels of kinetic energy at low temperatures as a coating technique. Takacs et al. observed that plates attached to inner walls of the crucibles can be coated with the powder charge and in some cases the powder may fuse into the substrate [33]. This method was successfully utilized in several recent studies showing homogenous coating on the surfaces of several substrates [34] [35]. This method has an advantage as an energy saver over other techniques used for coating surfaces with magnetic coatings such as electroplating [36] and laser-assisted heating [37].

Materials in general are categorized into 5 different classes in terms of magnetism, where each class reacts differently when exposed to a magnetic field. Paramagnetic and Diamagnetic materials react momentarily by arranging the internal field either parallel or opposite to the field [38]. In simple words, paramagnets get weekly attracted to a magnet and diamagnets would be weekly repelled. Ferromagnets on the other hand have the unique property of being attracted to a magnet and staying magnetic when removed from a magnetic field. These different behaviors of materials are associated with electrons and are explained by microscopic theory of magnetism [39].

The binary metastable Fe-Cu alloy has been the topic of several research efforts during the last few decades [40] [41] [42]. This is due to its interesting mechanical [34], electrical, thermal and magnetic properties [43] [44] [45]. Liu et al. [46] described the formation of the icosahedral phase of Fe-Cu alloy as unusual in the 1990 work discussing its magnetic and thermal properties. The material was proved to have a significant impact on the surface properties such as the hardness when applied as a coating layer [47]. Moreover, it has a unique magnetic behavior as reported by Drbohlav and Yavari [48] in 1995, showing a ferromagnetic property at room temperature for the $Fe_{50}Cu_{50}$ composition.

2.2   Theoretical Background

The working principal of the proposed system relies on the change in the static and dynamic responses of a cantilever beam resulting from the adsorption of contaminants by the coating material. These designs has been commonly used in the available literature on sensors, especially miniaturized ones allowing researchers to

develop a wide variety of devices that are capable of detecting explosives [49], pressure sensing [50], energy harvesting [51] and biological mass sensing [52] [53].

$$\Delta z = 4 \left(\frac{l}{t} \right)^2 \frac{(1-v)}{E} (\Delta \sigma_1 - \Delta \sigma_2)$$

- Δz = deflection of the free end of the cantilever
- L = cantilever length
- t = cantilever thickness
- E = Young's modulus
- v = poison's ratio
- $\Delta \sigma_1$ change in surface stress on top surface
- $\Delta \sigma_2$ change in surface stress on bottom surface

$$f = \frac{1}{2\pi} \sqrt{\frac{k}{m}}$$

$$\Delta m = \frac{k}{4\pi^2} \left(\frac{1}{f_1^2} - \frac{1}{f_o^2} \right)$$

- k = spring constant
- m = mass of cantilever
- f_o = unloaded resonant frequency
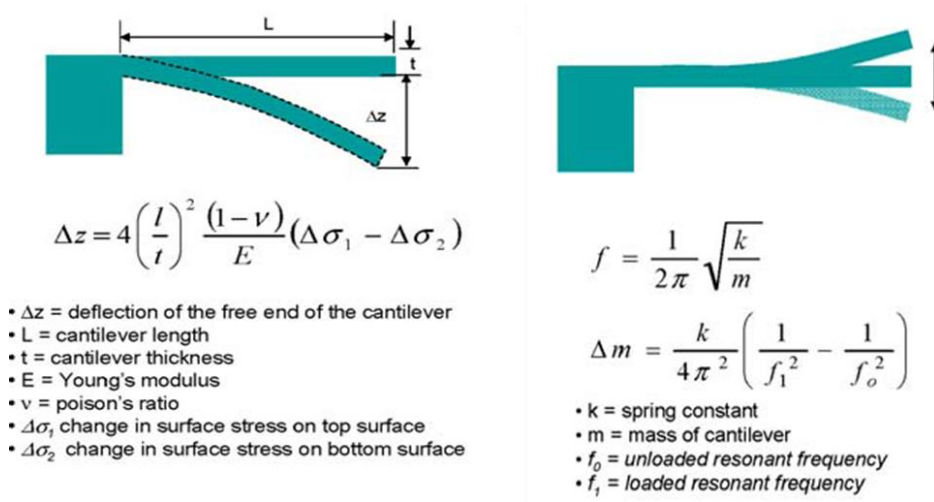- f_1 = loaded resonant frequency

Figure 4 Schematic comparing between static and dynamic modes of detection [54].

2.2.1 Mass detection modes. There are two well established modes for the detection of mass utilizing a cantilever beam structure. In the first method, the static deflection of a cantilever beam due to an added mass is measured and the mass leading to this deflection is calculated (static mode). This sensing mode relies on the change in surface stresses where the upper surface of the cantilever beam experiences higher tension and the lower surfaces experiences higher compression, where the larger mass results in higher deflection. The other method is based on detecting the shift in the natural frequency of a beam oscillating at its resonance due to its mass increase [54]. This is referred to as the dynamic mode. The natural frequency can be obtained by conducting FFT analysis of the dynamic response of the beam. The schematic in Figure 4 presents a comparison between the static and dynamic modes for mass detection utilizing a cantilever beam. The natural frequency of a vibrating structure ω_0 can be expressed as

$$\omega_0 = \sqrt{\frac{k}{m_0}} \text{ (rad/s)} \qquad (1)$$

where k is the stiffness of the structure and m_0 is its mass. After the addition of a mass Δm to the surface, the natural frequency of the system (denoted by ω_1) will depend on the original mass m_0 and the added mass Δm as follows.

$$\omega_1 = \sqrt{\frac{k}{m_0 + \Delta m}} \tag{2}$$

The added mass can be then estimated from the frequency shift as.

$$\Delta m = k\left[\frac{1}{\omega_1^2} - \frac{1}{\omega_0^2}\right] \tag{3}$$

The aforementioned expression of the added mass is a rough estimation based on a simple representation of the vibrating beam.

2.2.2 Mathematical model of vibrating beams immersed in fluid media. The mathematical model governing the bending of a thin cantilever beam vibrating in fluidic media (air and water) is formulated in this section. The beam is of length l, width b, and thickness h placed at a gap distance d from a laser sensor and submerged in fluidic medium. The beam is actuated by a mini shaker attached to its clamped end (base excitation). It is coated with a detector material selective to a target analyte present in the medium (ferrous contaminants). The attraction of particles by the coating material increases the effective mass of the sensor. The resulting shift in the resonant frequency Δf of the vibrating beam is used to detect the presence or concentration of the ferrous contaminants in the media. Figure 5 shows a schematic of the proposed beam with the functional coating and the attracted iron particles under base excitation.
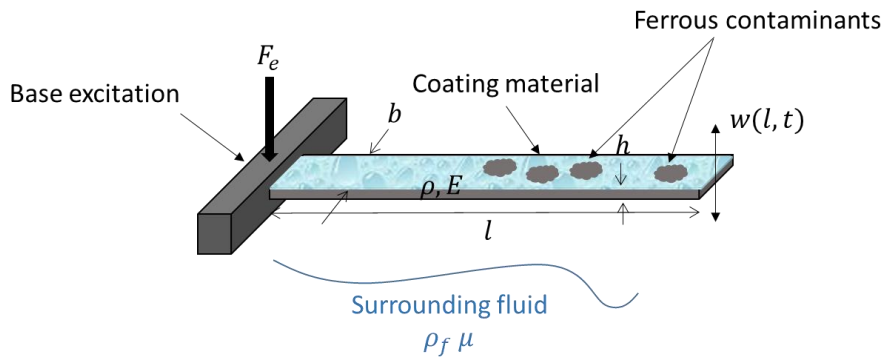

Figure 5 Schematic of the sensing beam under base excitation

Following Euler-Bernoulli beam assumptions and accounting for the added mass A_m, the dissipation mechanisms (structural and hydrodynamic damping), and the base excitation, the equation of motion governing the transverse deflection $w(x)$ of the sensing beam is expressed as:

$$\left(\rho bh(1 + A_m) + \frac{m_f}{l}\right)\frac{\partial^2 w(x,t)}{\partial t^2} + (c_s + c_h)\frac{\partial w(x,t)}{\partial t} + \frac{E}{1 - v^2}I\frac{\partial^4 w(x.t)}{\partial x^4}$$
$$= F_e(t) \tag{4}$$

where ρ is the beam density, m_f is the total mass of the coating material and ferrous contaminants, c_s and c_h denote the structural and hydraulic damping coefficients, respectively, E denotes the Young's modulus, v denotes the Poisson's ratio and I is the second moment of area of the beam. The excitation force is proportional to the base acceleration as:

$$F_e(t) = -m\frac{d^2 y}{dt^2} \tag{5}$$

$m = \rho bh(1 + A_m) + \frac{m_f}{l}$ denotes the total mass per unit length. The base is assumed to be subject to harmonic actuation in the form of

$$y(t) = Y\cos(\Omega_e t) \tag{6}$$

Y and Ω_e denote the amplitude and frequency of the base excitation. The added mass coefficient A_m and the hydraulic damping coefficient c_h are given by [55]

$$A_m = \frac{1}{\rho bh}\frac{\pi\rho_f b^2}{4}\left(a_1 + a_2\sqrt{\frac{2\mu}{2\pi f\rho_f b^2}}\right) \tag{7}$$

$$c_h = \frac{\pi\rho_f b^2}{4}2\pi f\left(b_1\sqrt{\frac{2\mu}{2\pi f\rho_f b^2}} + b_2\frac{2\mu}{2\pi f\rho_f b^2}\right) \tag{8}$$

where $a_1 = 1.0553, a_2 = 3.7997, b_1 = 3.8018, b_2 = 2.7364$. ρ_f and μ are the density and viscosity of the surrounding fluid, respectively. f is the natural frequency of the vibrating beam immersed in the fluidic domain (air or water). This frequency is the solution of the following nonlinear algebraic equation [55] :

$$f - \frac{f_v}{\sqrt{1 + \frac{1}{\rho bh} \frac{\pi \rho_f b^2}{4} \left(a_1 + a_2 \sqrt{\frac{2\mu}{2\pi f \rho_f b^2}} \right)}} = 0 \tag{9}$$

Here, $f_v = \frac{\beta^2}{2\pi l^2} \sqrt{\frac{EI}{\rho bh}}$ is the natural frequency of the beam in vacuum and β indicates the mode number.

Following the single-mode Galerkin approach, the beam deflection is approximated by:

$$w(x,t) \cong \varphi(x)q(t) \tag{10}$$

where $\varphi(x)$ is the mass-normalized mode shape of the cantilever beam and $q(t)$ is the modal coordinate. The mode shape $\varphi(x)$ is expressed as:

$$\varphi(x) = \sqrt{\frac{1}{mL}} \left[\cosh\left(\frac{\lambda x}{l}\right) - \cos\left(\frac{\lambda x}{l}\right) - \sigma\left(\sinh\left(\frac{\lambda x}{l}\right) - \sin\left(\frac{\lambda x}{l}\right) \right) \right] \tag{11}$$

In the present study, the vibrations of the cantilever beam near the primary resonance (first mode) is considered. As such, $\lambda = 1.87510407$ and $\sigma = 0.734095514$. Figure 6 shows the first three vibration mode shapes $\varphi(x)$ of a cantilever beam with 50 mm length and 0.4 g mass. The corresponding values of the parameters λ and σ are given in Table 1.
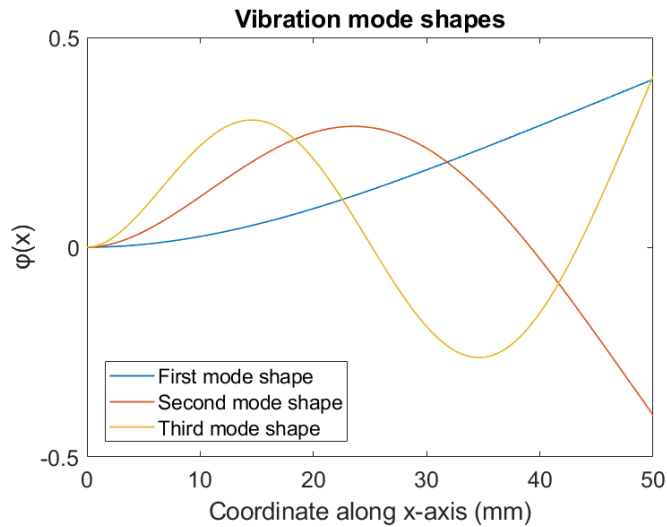

Figure 6 Vibration mode shapes of a cantilever beam.

24

Table 1 Values of λ and σ for the first three mode shapes.

Mode number	λ	σ
1	1.875	0.7341
2	4.694	1.0185
3	7.855	0.9992

Substituting Equation (10) in Equation (4), multiplying by the mode shape φ, and integrating the result from 0 to l, the following ordinary differential equation is obtained

$$\frac{d^2q}{dt^2} + 2\xi\omega_n\frac{dq}{dt} + \omega_n^2 q = \left(mY\Omega_e^2 \int_0^l \varphi(x)dx\right)\cos(\Omega_e t) \tag{12}$$

ω_n is the natural frequency (in rad/s) and $\xi = \xi_s + \xi_h$ is the total damping ratio. The damping coefficient is expressed in terms of the natural frequency and damping as follows:

$$c = c_s + c_h = 2m\xi\omega_n \tag{13}$$

Equation (12) can be solved numerically or analytically.

The beam tip deflection amplitude is given by

$$w_l = \left|\frac{mY\Omega_e^2 \int_0^l \varphi(x)dx}{\omega_n^2 - \Omega_e^2 + 2j\xi\omega_n\Omega_e}\right| \varphi(l) \tag{14}$$

where j is the unit imaginary number.

The developed code used for solving the equations presented is added to the Appendix section of this work. The simulation results along with the verification of the above model will be presented in Chapter 5.

Chapter 3. Experimental Methodology

In this chapter, the experimental methodology is discussed, including the development of the proposed sensor, the characterization of the coating material and the implementation of the testing setup. Figure 7 shows a schematic summarizing the experimental methodology involving three main steps, namely: synthesis of the sensing material, coating the substrate, and analysis of the response of the sensor using the developed experimental set-up.
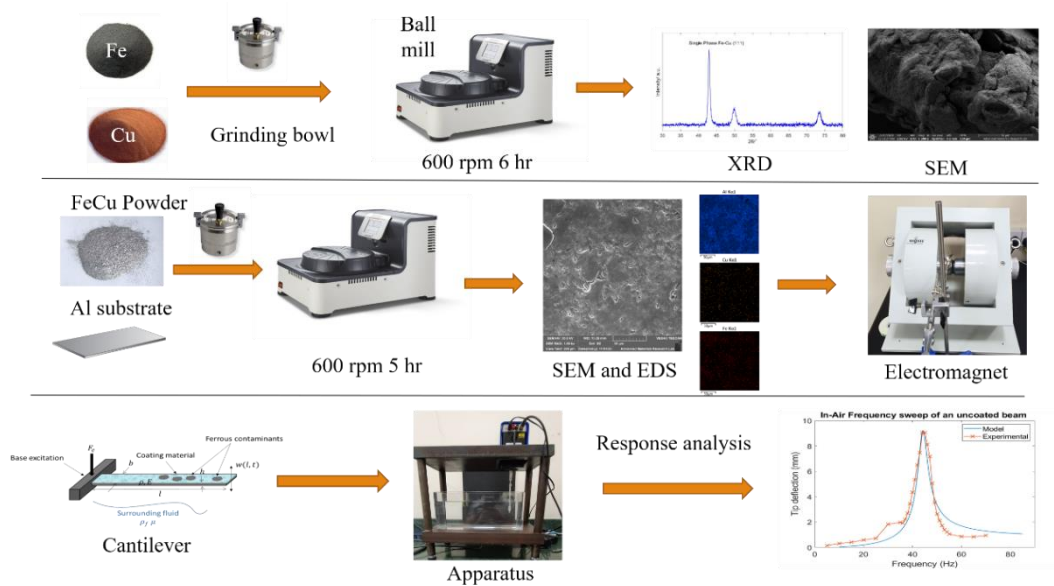

Figure 7 Schematic summarizing the experimental methodology.

3.1 Synthesis of the Coating Material

The Fe-Cu powder is prepared via mechanical alloying of the precursors (iron and copper powders used as received from Segma-Aldrich) in the Fritsch premium line Pulverisette 7 planetary ball mill. This type of ball mills is the most commonly used as it provides the required speed ratios, ball-powder orientation, and capable of grinding a variety of materials in both wet and dry operation modes. The parameters of the dry ball milling process are fixed at 600 rpm of milling speed, for 6 hours duration with a 30-minute break between each hour. As for the ball-to-powder ratio, it is fixed at 6:1 using 10 mm diameter stainless steel balls, and the powders are added in 1:1 mass ratio.

This process provides the required energy –in the form of collisions- which allows the interdiffusion between the Fe and the Cu particles to happen creating a new solid-state solution. As the mass ratio is sat to be 1:1, the outcome of this processes is the metastable single-phase $Fe_{50}Cu_{50}$ alloy. The development of this material, along with the intermediate phases it undergoes is further explained when discussing the X-Ray diffraction in Section 3.4.1 of this study. Finally, it is worth to mention that this process can be upscaled by using high-pressure blasting to coat bulk quantity of aluminum sheets [56] [57] .

3.2   Substrate Coating Technique

The coating technique used in this study utilizes the kinetic energy of the small particles inside the ball milling machine to create a coating layer on the aluminum substrate. For the purpose of experimentally testing the effect of the coating thickness and structure on the behavior of the produced samples, several sets of parameters are tested by varying the milling speed and time, while fixing the quantity of powder used to coat the substrate. Four milling speeds starting at 200 rpm, up-to 800 rpm are mainly tested while the milling time was varied from 1 to 5 hours. Moreover, the mass of the powder used to coat the substrate is fixed to be 3 grams which allows a consistent comparison between the two previously mentioned process parameters.

3.3   Magnetization Technique

To magnetize the thin ferromagnetic layer coated on the aluminum substrate Weistron Programmable Electromagnet shown in Figure 8 is used. This is done by placing the coated samples in a constant magnetic field. The electromagnet with 4 Ohm coil resistance and maximum power of 1500W is used to generate a 1 Tesla magnetic field between the two iron cores where the coated sample is placed for 10 minutes.

Figure 8 Weistorn Programmable Electromagnet.

3.4 Characterization Techniques

3.4.1 X-ray diffraction. X-Ray Diffraction (XRD) is used to insure the sufficient inter diffusion of the binary Fe-Cu alloy and the formation of the single-phase form. The XRD patterns are recorded in the 2θ geometry where time and step size are specified as input parameters. The XRD apparatus used in this study is Bruker D8 Advance DaVinci multipurpose X-ray diffractometer with Cu Kα radiation operating at λ = 1.5406 Å, 40 kV tube voltage and 40 mA current. Alami et al demonstrated the successful synthesis of Fe-Cu after 6 hours of milling, showing the development of the XRD patterns in as illustrated in Figure 9 [58]. In the As-is state, peaks indicating the existence of the BCC iron and FCC copper are both present. However, as can be seen in Figure 9, as the milling process starts, changes in the microstructure start to occur until a final state is reached after 6 hours of milling where the only peaks that exist are representative of the single-phase metastable FCC Fe-Cu alloy.
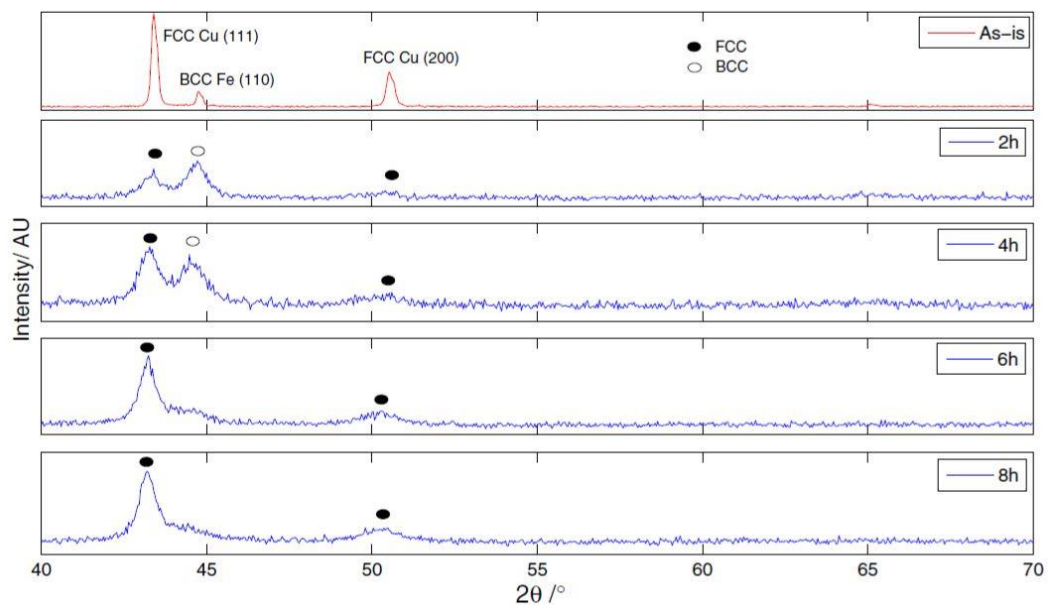

Figure 9 XRD results of the development of the single-phase Fe-Cu [58].

3.4.2 Scan electron microscope /energy-dispersive x-ray spectroscopy. Scanning Electron Microscope (SEM) and the coupled Energy Dispersive X-ray Spectrometer (EDS) are used to characterize the surface properties of the coated samples to enable visualizing the structure of the coating and the distribution of the elements within the inspected area. SEM and EDS can also be utilized as tools for

measuring the thickness of the coating using cross sectional imaging by SEM or the thickness analysis via EDS. The SEM used in this work is VEGA3 XM by TESCAN, operating at 5 kV, while the EDS analysis is conducted with both map and point modes at the same operating voltage.

3.5 Assessment of Magnetization

In order to quantify the mass added to the coated beam samples post the magnetization process the samples are weighed, dipped in iron powder and shook to remove any excess powder that is not attached to the beam by magnetic attraction. Afterwards, the beams with the attached iron powder masses are measured using RADWAG analytical scale with a resolution of 0.0001g and linearity error of ± 0.2 mg and the mass of the beam is subtracted. The beam is later cleaned from the powder and preserved for the same process to be repeated over four days to assess the duration within which the coating can preserve the magnetic behavior.

Chapter 4. Experimental Testing Set-up

As mentioned in the theoretical background section of the Thesis in Chapter 2, there are two main methods of utilizing the tip deflection of a cantilever beam as a sensing method, namely, the static and dynamic modes. The static mode relies on detecting the added mass, resulting from the iron intake, from the static deflection of the free end of the beam while the dynamic mode relates the resultant shift in the natural frequency of the vibrating beam to the added mass. This chapter discusses the development of the experimental set-up to test the capabilities of the coating material deposited on the vibrating beam to detect the presence of iron in aqueous media.

4.1   Set-up construction and components

The working principle of the proposed iron sensor is based on the vibration of the coated beam samples operating at resonance to amplify the output signal, where the actuation of the system is carried out via base excitation from an outer source (mini shaker). The captured iron particles will result in adding mass to the system and then causing a shift in the natural frequency. Both the dynamic and the static modes are studied in this work. The static mode is assessed by adding a known mass of the iron powder to the selected beam with 5 mg increments while recording the deflection of the beam's tip.

For the dynamic mode, the prepared samples of aluminum substrates (treated as cantilever beams under base excitation) with the magnetized ferromagnetic Fe-Cu coating are utilized for sensing iron in aqueous solutions. The beams are excited at varying frequencies while exposed to the test media. The Smart Shaker K2007E01 with 31 N output force,13mm stoke and 9 kHz frequency range with Integrated Power Amplifier by The Modal Shop is used to excite the beam at the desired frequency. An arbitrary waveform generator with advance signal generator function, namely Rigol DG1032Z, is used to perform a frequency sweep near the primary resonance. The tests are conducted in air, and in pure Deionized water (DI) for both coated and uncoated beam samples.

Figure 10 shows the CAD model and the actual the experimental testing set-up which is supported by the illustrated mounting structure designed to house the shaker, transparent water container, and the Baumer OM70 laser point / laser line distance

sensor which is used to measure the tip deflection as the beam is subject to base excitation.
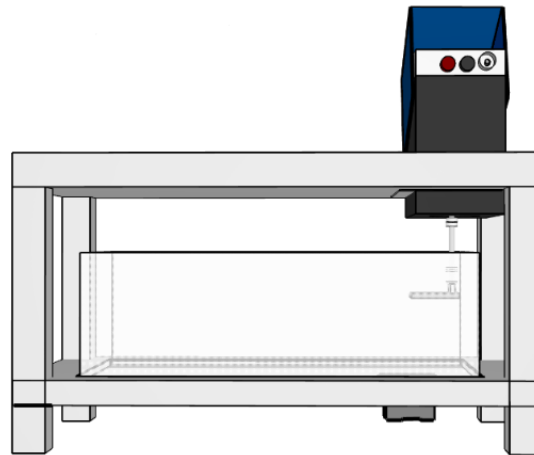
(a) CAD model
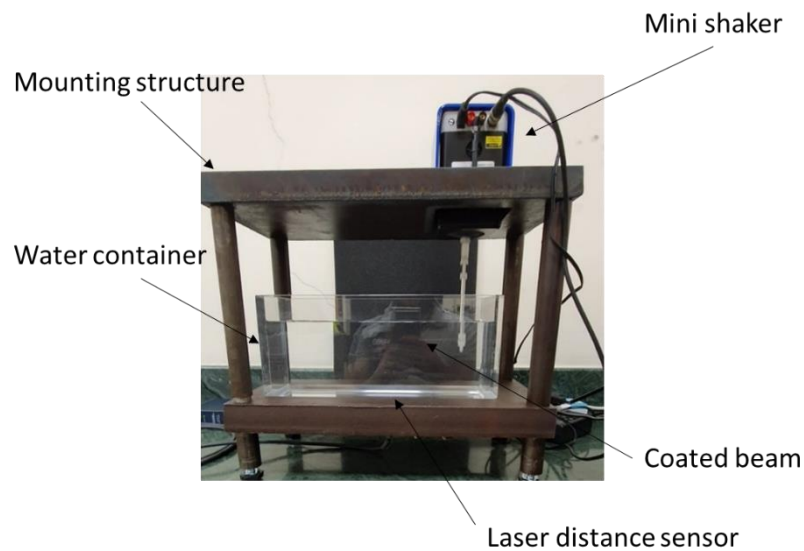
(b) Actual sensing set-up

Figure 10 Schematic of the experimental set-up: (a) CAD model, (b) actual set-up.

4.2 Laser Sensor Connection and Communication

The Baumer laser point/laser line distance sensor is used to measure the tip deflection in the experimental set-up of this work. The sensor is a tested and certified equipment with a pulsed red laser diode generating a 660nm wavelength class one laser. The resolution of the device varies based on the set-up and the tested target is within a

range from 1.4 to 6.3µm when the highest precision filter is used and from 5.3 to 25µm without deploying a filter as per the technical specifications. The response delay time also depends on the mode of operation. It is 0.8 ms for single shot measurements and 1.2 ms for continues operation. The measuring frequency of the sensor is 2500 Hz.

In order to operate the sensor as per the intended experiments, it needs a 15-28 VDC power supply. Moreover, to be connected with a computer for data acquisition and processing, the communication takes place through an RS485 output which requires the use of an RS485 to USB/Ethernet converter. StatTech 1 Port industrial USB to RS422/RS485 serial adapter is used for this purpose. In addition, H-term freeware is used as a user interface for communicating with the sensor using ASCII and HEX communication protocols. Figure 11 shows the connection schematic of the sensor with the converter and the power supply. Moreover, Figure 12 displays the actual circuit that connects the sensor, power supply, RS485 to USB adapter and the computer.
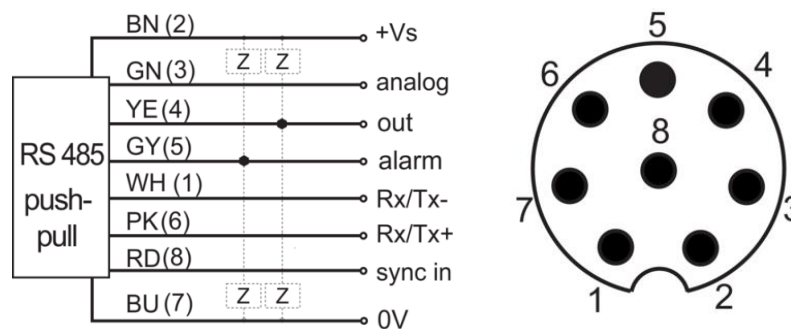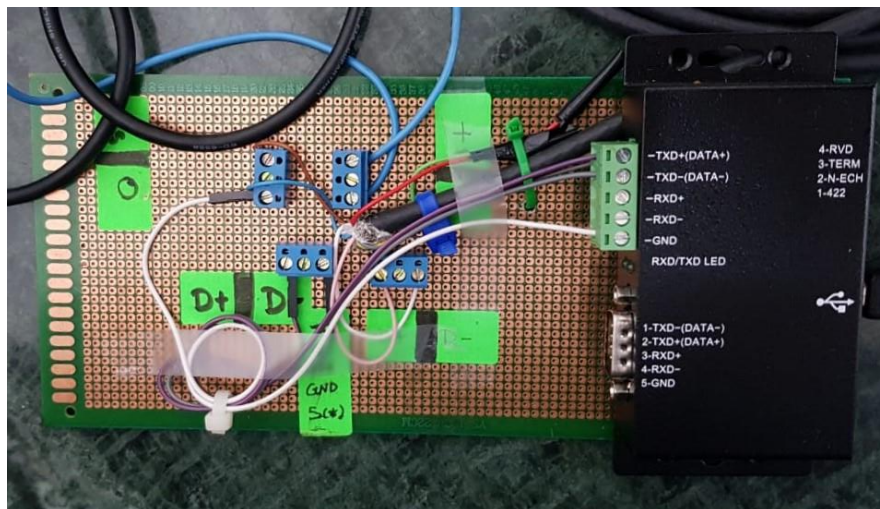

Figure 11 Sensor connection schematic.

Figure 12 Actual connection circuit with the laser sensor.

Chapter 5. Results and Discussion

In this chapter, microstructural characterization results are presented along with the experimental and numerical results obtained for the proposed iron sensor.

5.1 Experimental Results

5.1.1 Microstructural characterization.

5.1.1.1 XRD. One important step that indicates the success of the desired Fe-Cu phase is X-Ray diffraction. Frequent samples are taken from the grinding bowls and tested in the XRD machine to assess the resulting peaks that are indicative of the degree of interdiffusion. Figure 13 displays the obtained XRD results of the prepared Fe-Cu powder. These XRD results confirm the presence of a single peak at 43º and then the formation of single-phase Fe-Cu is ensured, and milling can cease.
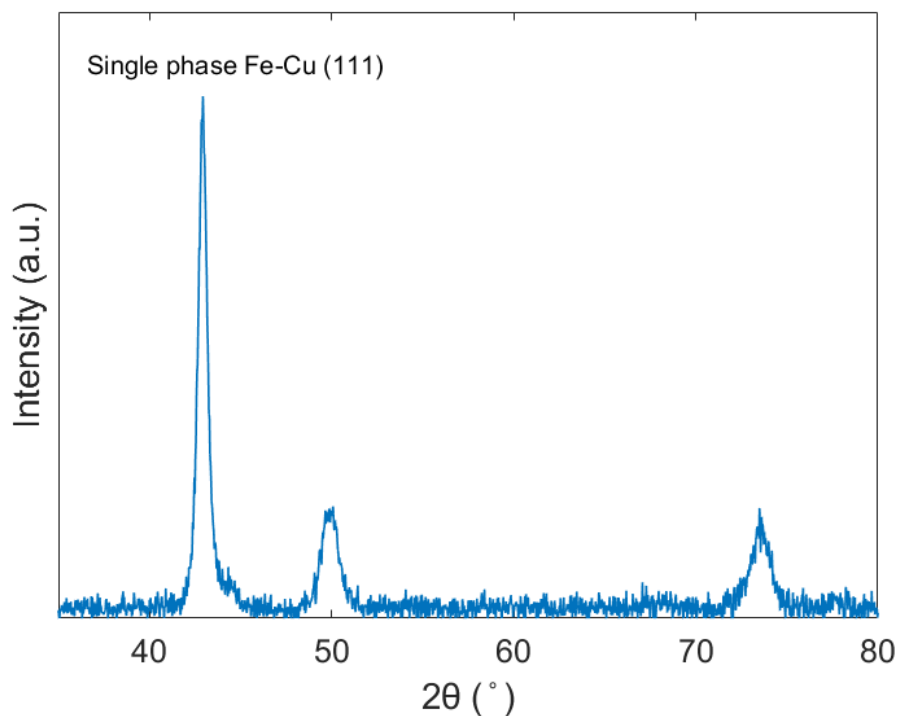

Figure 13 XRD results of the prepared Fe-Cu powder.

It is worth to mention that since the metastable Fe-Cu alloy is naturally immiscible at room temperature, heating the sample results in the dissociation of the alloy. And hence, the reappearance of two peaks at 43º. Figure 14 shows the XRD

pattern of the Fe-Cu powder after heating at 500 ºC which is the temperature of the dissociation [58]. Another observation that is noticeable from Figure 13 is the formation of iron oxide, which is mainly due to heating under ambient conditions.
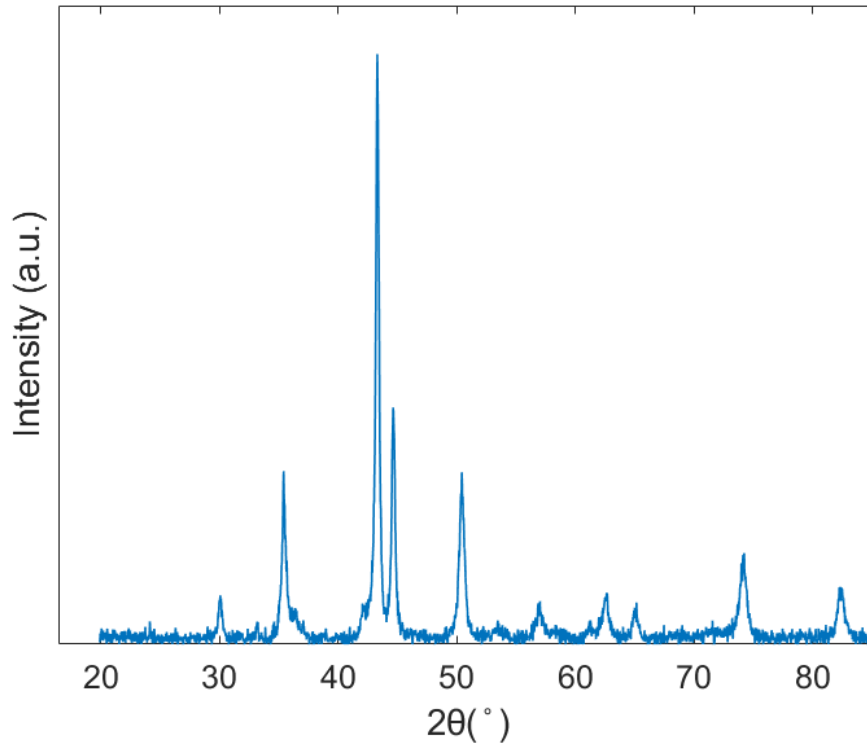

Figure 14 The dissociation of Fe-Cu powder after heating at 500 ° C.

Moreover, the XRD patterns of the aluminum beams coated with the Fe-Cu can be used to confirm the integrity of the coating material after the coating process is over. This helps to assess the effect of the coating process on the microstructure of the alloy. However, since the coating thickness is below 500 nm as reported in the following section of this study and the intensity of the peaks will be dominated by the aluminum substrate. Therefore, a sample with higher coating thickness (around 2µm) was prepared for the purpose of confirming that the coating technique has no effect on the final structure, but this sample is not further used in this study. Figure 15 shows the XRD pattern of the Fe-Cu coated Al beam where both the 43º and the 50º peaks co-exist with the aluminum peaks from the substrate.
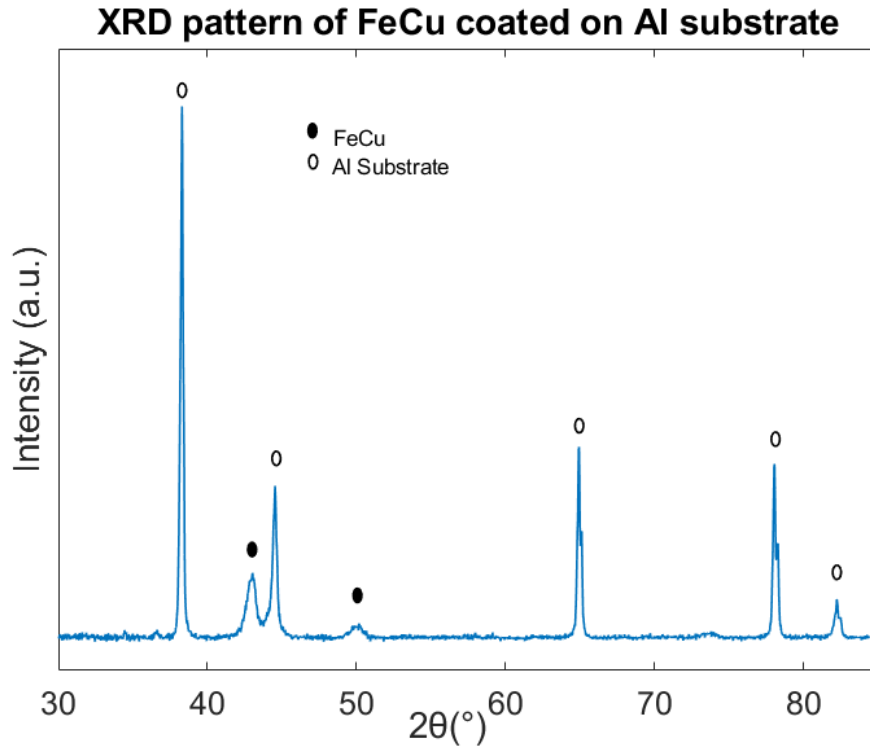
Figure 15 XRD pattern of aluminum substrate coated with the Fe-Cu powder.

5.1.1.2 SEM/EDS.

5.1.1.2.1 powder analysis: The SEM images in Figure 16 show the Field Emission SEM of the synthesized Fe-Cu by mechanical alloying via dry ball milling as explained in Chapter 3. There are two interesting observations that can be concluded form these images. First, the size variation of the resulting powder is significant, where some of the particles are around 50 µm in size and the size of others are below one µm. Second, the particles tend to cluster, and this is mainly due to the strong cohesive forces of the particles, which can be emphasized in the presence of even weak magnetic fields due to the magnetic nature of Fe. The clustering of the Fe-Cu powder due to the nature of the material and the synthesis process used gives an advantage to the coating method utilized in this study as it relies on the kinetic energy of the moving powder. However, in cases where a finer powder is required a second size reduction step is added after the alloying process is done by further milling with smaller diameter balls.
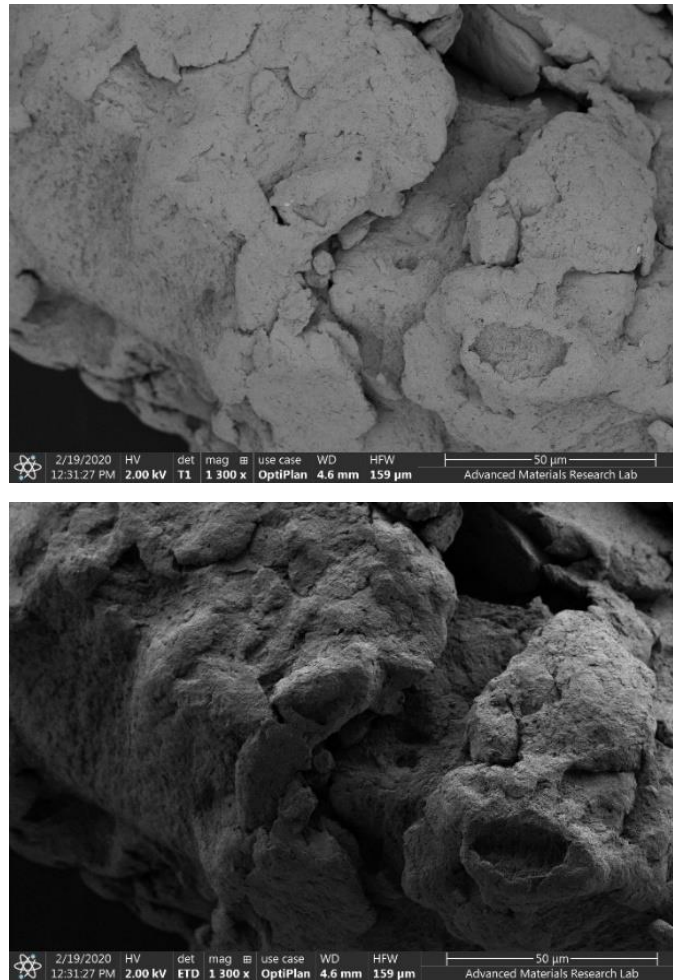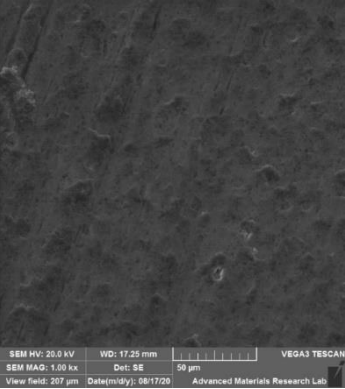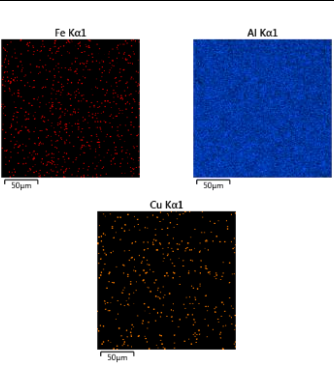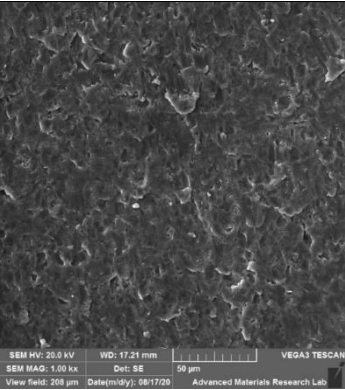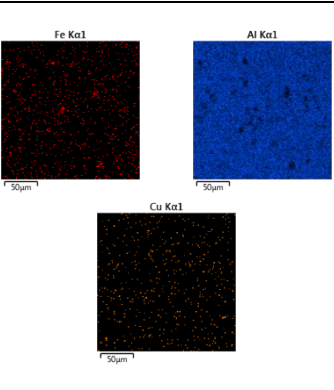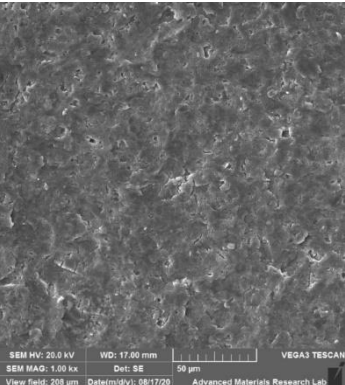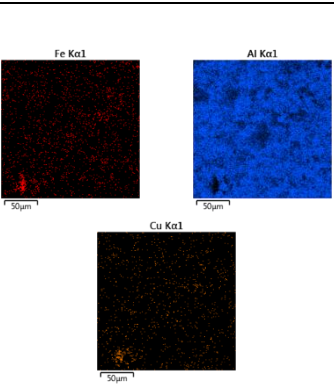
Figure 16 FE-SEM images of the Fe-Cu powder using two different sensors.

5.1.1.2.2 coating homogeneity and thickness: The Fe-Cu coating will introduce the desired magnetization effect to the paramagnetic aluminum substrates. It is expected that the homogenous distribution on the beam surface would result in even surface magnetization as well as good detection. The SEM, EDS and the coating thickness obtained via EDS of 6 different coated beam samples are summarized in Table 2. The samples are prepared at different coating parameters with milling speed varying from 200 to 600 rpm as it was experimentally observed that coating samples at 800 rpm milling speed was destructive to the thin aluminum substrates as shown in Figure 17 . The EDS results show a consistent trend of elemental mapping of the aluminum, iron, and copper, where the signal of the Al substrate is the most dominant and the Fe-Cu coating is distributed homogenously throughout the samples. Another important observation regarding the coating thickness is visualized in Figure 18 where the samples are divided into two sets based on the coating time (2 hours and 5 hours). Both

36

sets show an almost linear trend of increasing the coating thickness with increasing the milling speed. However, it is worth to mention that the factor at which the thickness increases with increasing the milling speed is higher for the 5 hours coating time set in comparison to the one obtained for 2 hours coating time. Moreover, at each milling speed considered in this study, the coating thicknesses of the samples coated for 5 hours are higher than those coated for 2 hours.

Table 2 SEM, EDS, and coating thickness of the produced coated beam samples.

Milling Parameters	SEM	EDS	Thickness (nm)
200 rpm 2hours			87.2
400 rpm 2hours			143.8
600 rpm 2hours			319
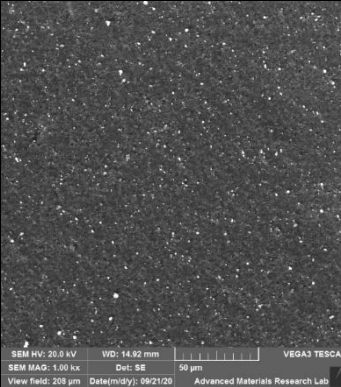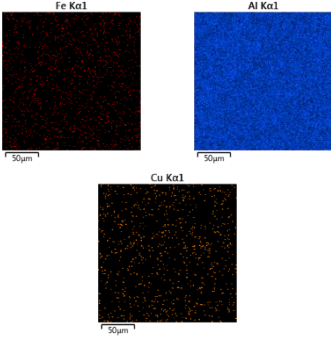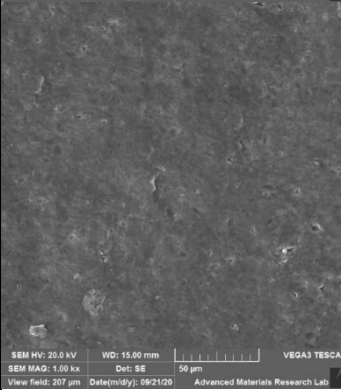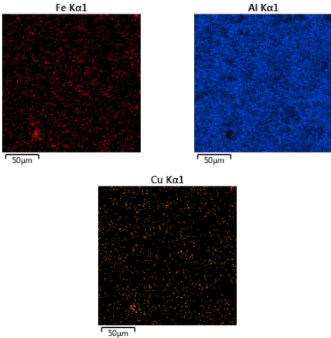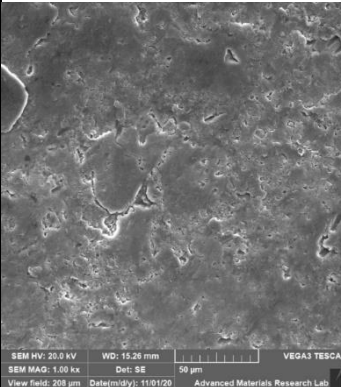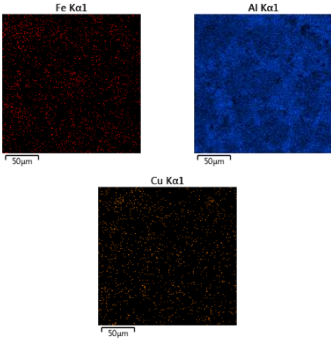
200 rpm 5hours			167.5
400 rpm 5hours			360.1
600 rpm 5hours			499.7

Figure 17 Sample affected by high energy coating at 800 rpm

38

Coating thinckness vs. The milling speed

Legend:
- × 2 hours
- ◇ 5 hours
- – – 2 hours fit
- – – 5 hour fit

$y5 = 0.83*x + 10$
$R^2 = 0.9916$

$y2 = 0.58*x - 48$
$R^2 = 0.9197$

X-axis: Milling speed (RPM)
Y-axis: Coating Thickness (nm)
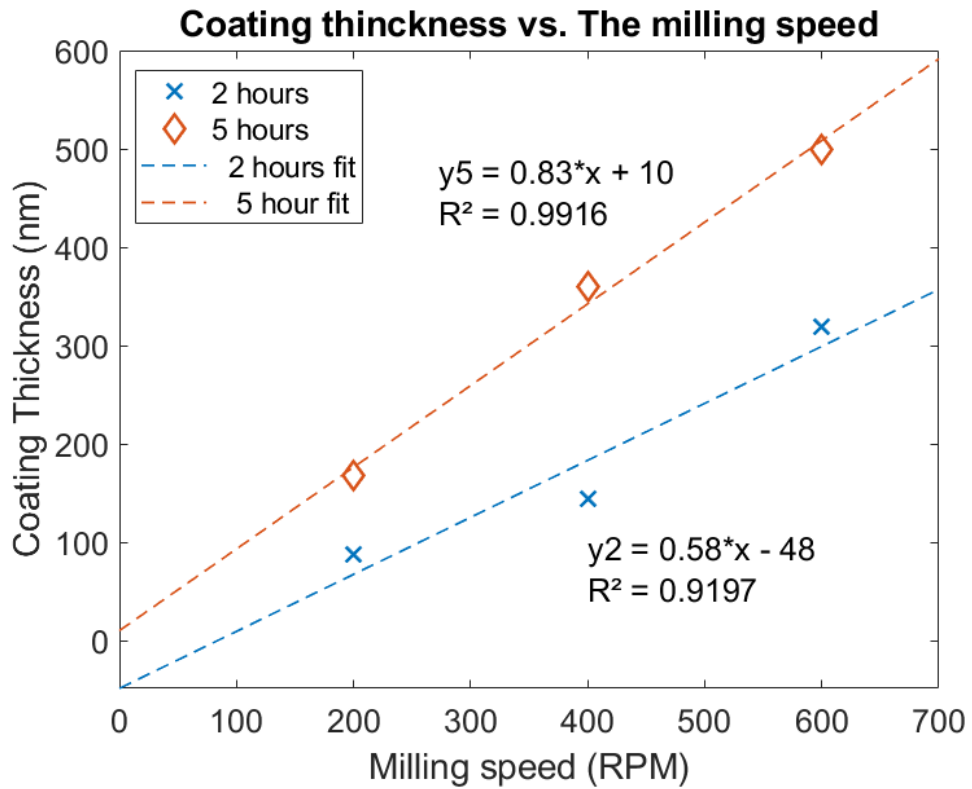
Figure 18 Variations of the coating thickness with the milling speed obtained for two sets of the beam samples (coating time of 2 hours and 5 hours).

5.1.2 Assessment of magnetization. To assess the magnetic behavior of the coated beams, the sample with the highest thickness is selected post the magnetization process mentioned in the Methodology chapter of the Thesis as it showed the best performance as a magnet when dipped in dry iron powder as illustrated in Figure 19 .
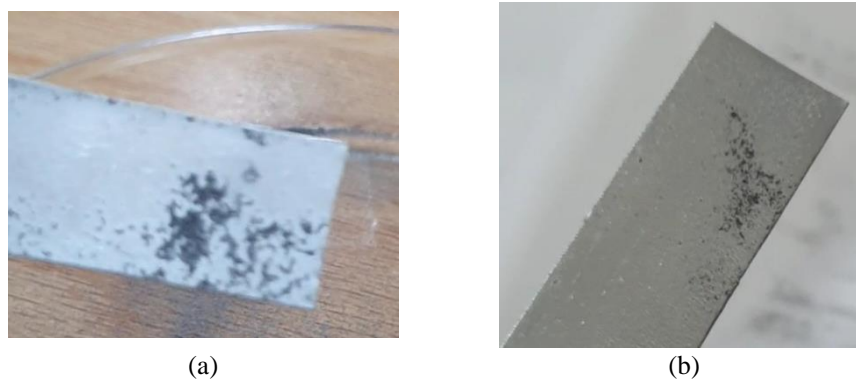
(a)   (b)
Figure 19 Iron attracted by the coated beam: (a) highest thickness and (b) lower thickness.

Figure 20 shows the behavior of the coated beam over the period of 4 days, where day one is the day the magnetization process took place. Here, the method of assessing the magnetic strength depends on measuring the mass of the powder that is attracted to the beam's surface where the area subjected to the powder is the first 200 mm^2 of the beam. The results show that in day 1 the amount of the attracted iron powder is 7 mg, and this is taken to be the maximum amount the beam can attract. The following days show a general decay of the strength until it reaches a constant value after the 3rd day. The slight increase in the attracted powder mass in the fourth day might be due to the accuracy of the used balance. That is, the difference between mass of the days 3 and 4 is around 0.7 mg and each point has an uncertainty of ±0.2 mg. Therefore, the attracted mass is considered to have reached a constant value of around 3 mg. This point can be further investigated by increasing the number of measurements per day and increasing the duration of the testing.
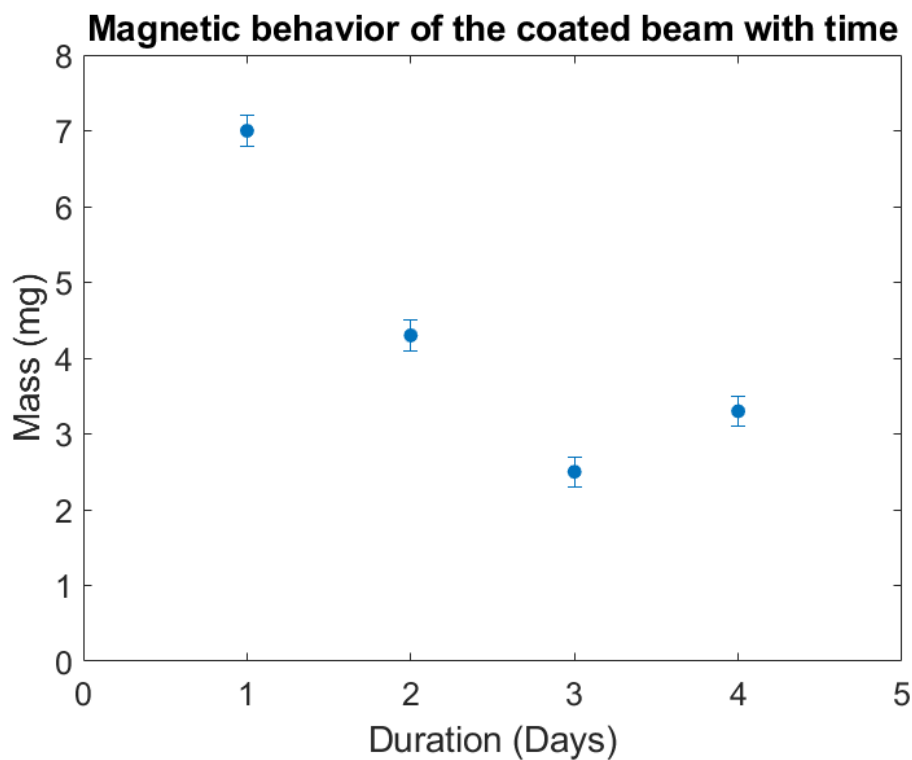
Figure 20 Mass of the captured iron powder by the coated beam after being dipped in dry iron powder with time (error bars define the balance uncertainty).

5.1.3 Dynamic and static detection modes results. As discussed earlier in the methodology chapter, both detection modes are studied in this Thesis. The geometry and material specifications of the beams under investigation are presented in Table 3.

Table 3 Specifications of the used beam samples.

Dimensions $l \times b \times h$ (mm^3)	Material	Form
$50 \times 10 \times 0.25$	Aluminum (mainly)	Flexible sheet

Figure 21 shows the distance data obtained from the sensor when mass is added in 5 mg increment. The results show an almost linear trend in the static tip deflection when mass is added. However, it is worth to mention that the illustrated results fall within the confidence limit of the used sensor and the obtained data can be affected by the linearity error. Hence, and taking a conservative assumption, the beam samples used in this study will be considered insensitive to masses less than 10 mg in the static mode which exceeds the maximum amount of powder that can be captured by the thin coating layer. This is mainly due to the geometry of the samples where more flexible beams can be designed with lower thicknesses and higher aspect ratios. Another approach to resolve this issue is to deploy a laser distance sensor with higher resolution or other measurement techniques (e.g., using piezoelectric patches made of microfiber composite) when measuring the static deflection.
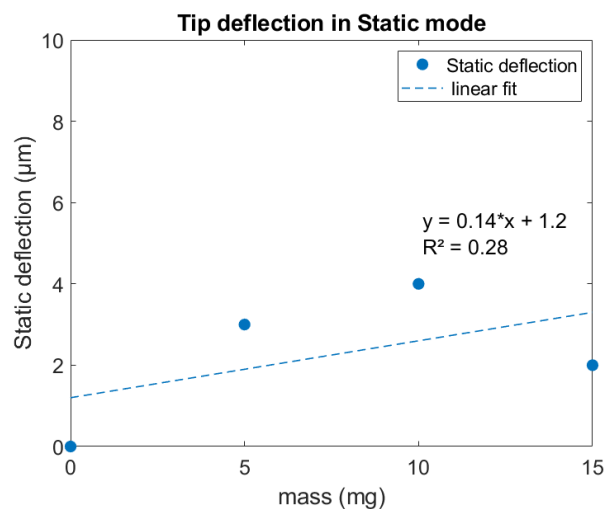
Figure 21 Results of the static mode detection showing data points within the confidence level of the laser sensor.

Dynamic mode testing was performed on uncoated beams in air and water along with a coated beam sample in water using the set-up shown in Figure 10 where the samples were attached to the mini-shaker's arm in a configuration that allows them to vibrate laterally as cantilever beams. Each experimental data point is obtained by taking the maximum value of 500 measurements captured at each frequency, which corresponds to the amplitude of vibrations. This corresponds to the operation at resonance that results in the maximum amplification in the beam vibrations. It is worth to mention that as per the distance laser sensor's data sheet, it has a sampling frequency of 2500 Hz and a response time of 1.2 ms. Figure 22 shows the 500 measurements of the oscillating beam at its natural frequency with the maximum value of 10.45 mm and a time step of 0.11 s. This sampling time difference between the sensors' specifications given in the technical sheet and the actual measurements is due to the used software and data converter deployed to communicate between the computer and the distance laser sensor. However, this does not affect the experimental procedure, as the output of interest is the amplitude of vibrations.
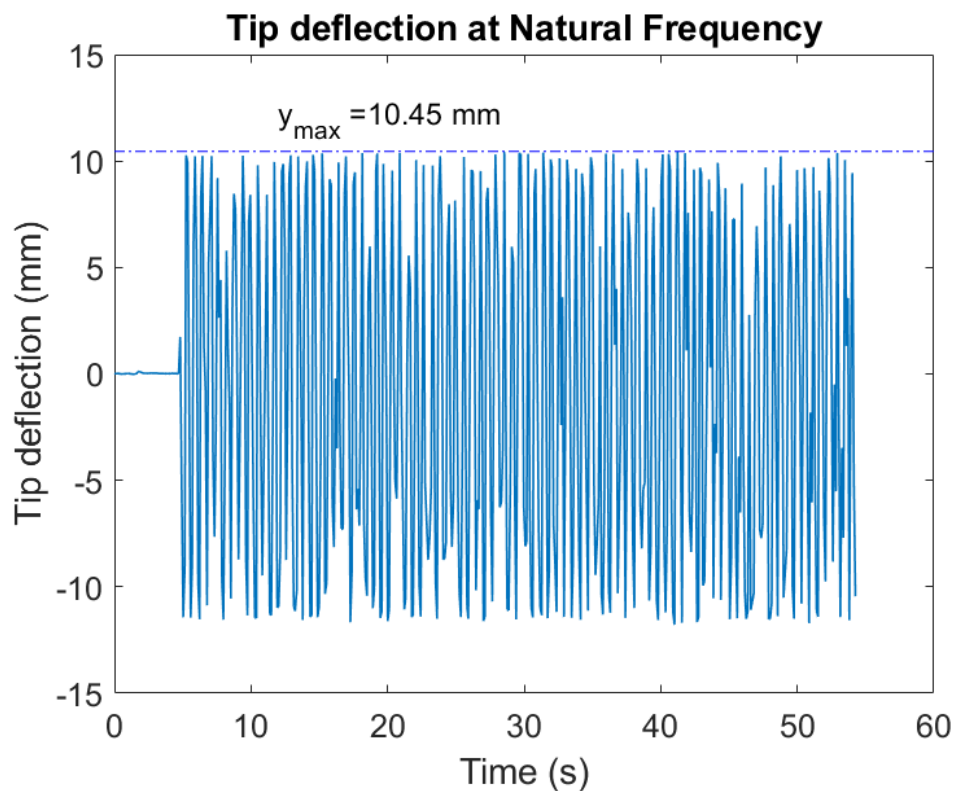
Figure 22 Time response of the beam oscillation at 44 Hz.

42

Moreover, the obtained values are corrected by subtracting the deflection values at the base to get the relative displacements. Indeed, since the beam samples are treated as cantilever beams, any deflection value due to the motion of the shaker's arm should be disregarded. It is noticeable form the results represented in Figure 23 that the values of the relative base motion decreases as the frequency increases in an almost linear manner. The amplitude of the base excitation is found experimentally to be 1.705 mm at the natural frequency of the system.
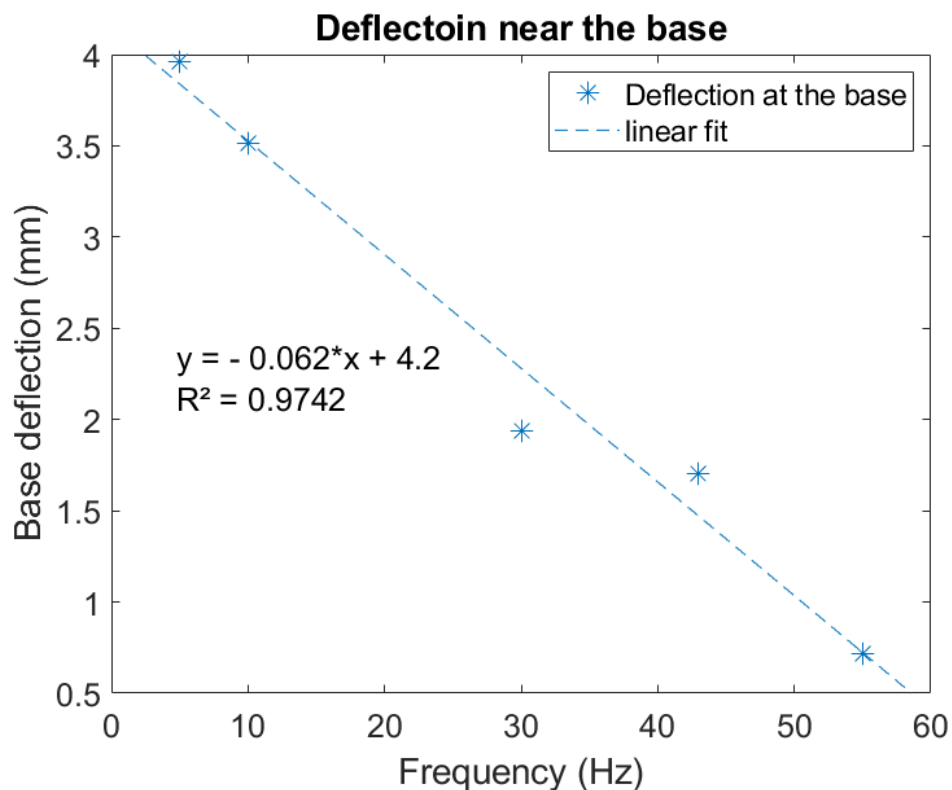
Figure 23 In-air deflection values near the base (each data point is the maximum value of 500 readings).

The results obtained from the frequency sweep are used to verify the model suggested in this study which is later implemented for the same cantilever beam to prove the functionality of the sensing approach. Figure 24 shows the comparison between the frequency response generated by the model (blue curve) and the results obtained experimentally (orange curve) when the beam is vibrating in air under varying excitation frequency controlled through the mini shaker. The comparison shows a good

agreement between the two sets of data and indicate an accurate prediction of the natural frequency around 44 Hz, as exhibited by the peak of the frequency response curve.
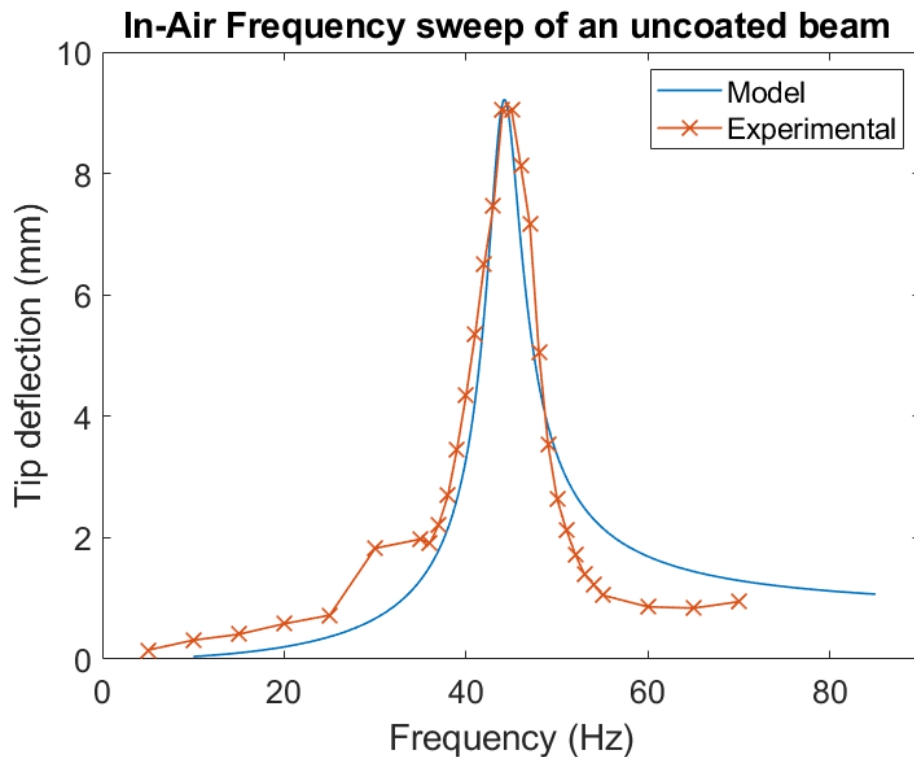
Figure 24 In air frequency response: a comparison between the numerical and the experimental results.

Similar to the in-air vibration results, the frequency responses of an uncoated Al beam along with a coated beam with a 360 nm coating layer submerged in DI water are measured over a range of frequencies starting form 1 Hz up-to 25 Hz with a 1 Hz step. Figure 25 shows that the natural frequency for both beams is around 7 Hz when vibrating in water. The shift in the natural frequency along with the reduction in the amplitude of the beam vibrations when shifting from air to water is illustrated further in Figure 26. This is a result of the added mass and damping of water compared to air. Moreover, both beams (coated and uncoated) show an almost identical trend due to the fact that the coated beam has only 360 nm of coating thickness and then resulting in an insignificant increase in the effective mass. On the other hand, keeping the same behavior proves that the beam keeps the same flexibility after coating and the hardening due to the coating method can be disregarded.
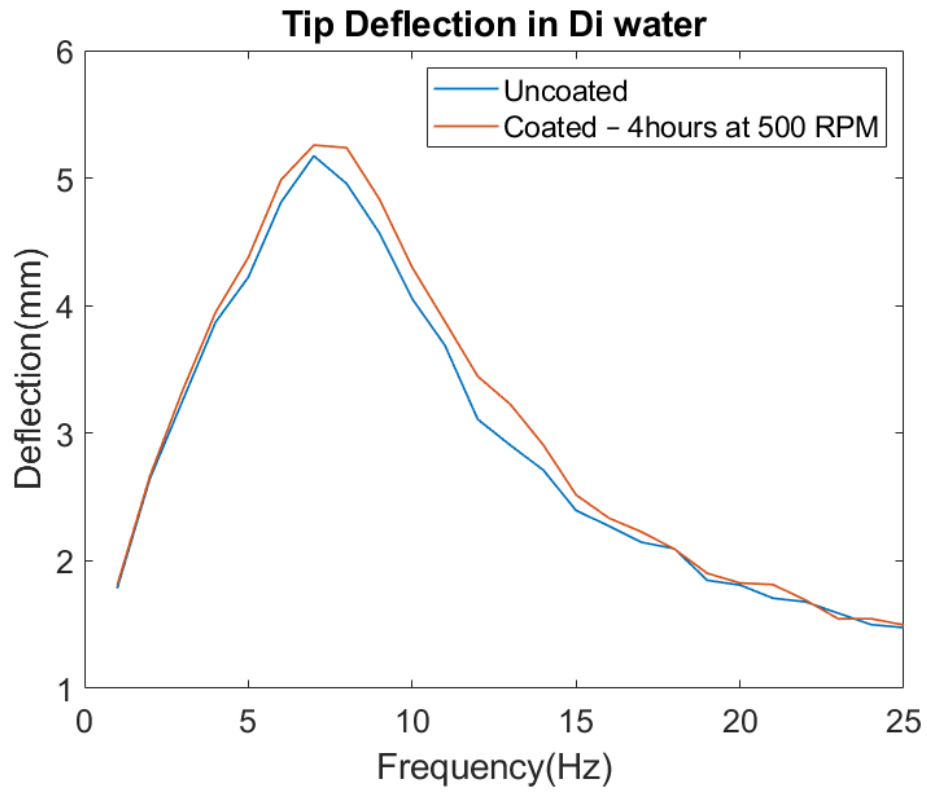
Figure 25 Experimental Frequency response of the coated and uncoated beams in Di water.
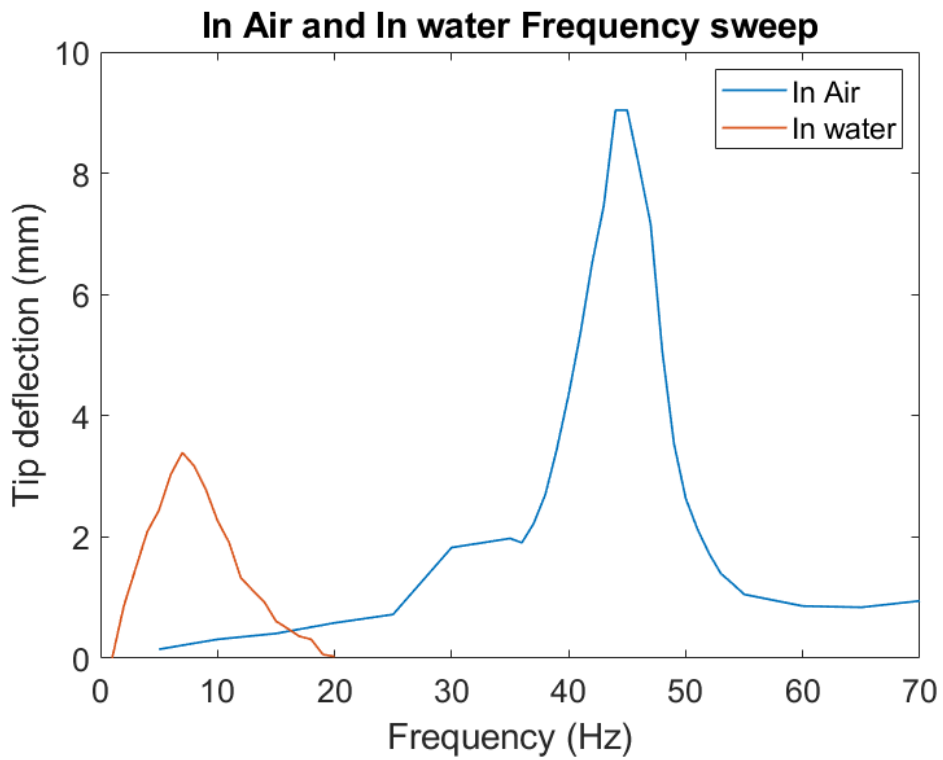
Figure 26 Experimental Frequency responses of the uncoated beams when vibrating in air and water.

45

When the study was taken further to the experimental assessment of the dynamic mode proposed for the detection of iron contaminants, several limitations were encountered. Some of them are related to the sensing method used in the experimental testing set-up constructed in this study. When the contaminates were introduced to the aqueous media, the laser distance sensor becomes ineffective due to the reflection of the laser beam when encountering the suspended iron particles. Other reasons are due to the physical capability of the sensing system such as the resolution of the current mini shaker is limited to 1 Hz which is insufficient in some cases such as illustrated in the next section. Moreover, the size of the used beam samples being is in the macro scale (surface area of 5 cm^2) makes the surface tension forces required to adhere the captured particles by the magnetic force not sufficient to withstand the vibrations of the beam when operating in dynamic mode. These issues can be resolved when scaling down the device the micro level and deploy other transduction techniques (e.g. capacitive-based or piezoelectric) that can detect beam deflections in the order of micrometers. Further modifications to the proposed sensing system may include the replacement of the substrate material with a porous metal foam, enhancements of the coating material, studying the effect of localized high-density coating points and heat treatment. These design modifications are elaborated in Chapter 6 of the Thesis as possible future work.

5.2   Simulation Results

In this section, a numerical analysis to verify the potential use of the dynamic mode for sensing the ferrous contaminants is conducted. This approach works by detecting the shift in the natural frequency that can be extracted from the peak of the frequency response of the vibrating beam. This numerical analysis is carried out using the model proposed earlier in Chapter 2 of this study after being validated experimentally as shown in Figure 24. However, in order to match the frequency response some tuning of the model parameters has been done by assuming some uncertainties in the physical and geometry properties of the beam samples under investigation where the Young's modulus and the damping coefficient of the beam were selected by matching the peak response at resonance. The dimensions and material properties of the beam are presented in Table 4. The amplitude of the base excitation Y is set to be 0.5 mm. Next, the deposition of ferrous contaminants on the beam is assumed using the maximum mass percentage noticed in Figure 20 which is around 2%

of the total mass of the beam. The resulting frequency response curves are shown in Figure 27. A frequency reduction from 7.73 Hz to 7.63 Hz is observed evident from the shift of the response peak to the left as a result of the softening effect of the added mass. This result indicates the need to use of a more sophisticated transduction technique with the capability to capture a frequency shift in the order of sub-Hz in order to effectively detect the expected amount of iron to be attracted by the coated beam. Other alternative to amplify the shift in the frequency resulting from added mass is to operate at higher modes [59]. Finally, the Mathematica code used to generate the frequency response of the dynamic mode following the proposed model is given in the Appendix of this work.

Table 4 Dimensions and material properties of the sensing beam

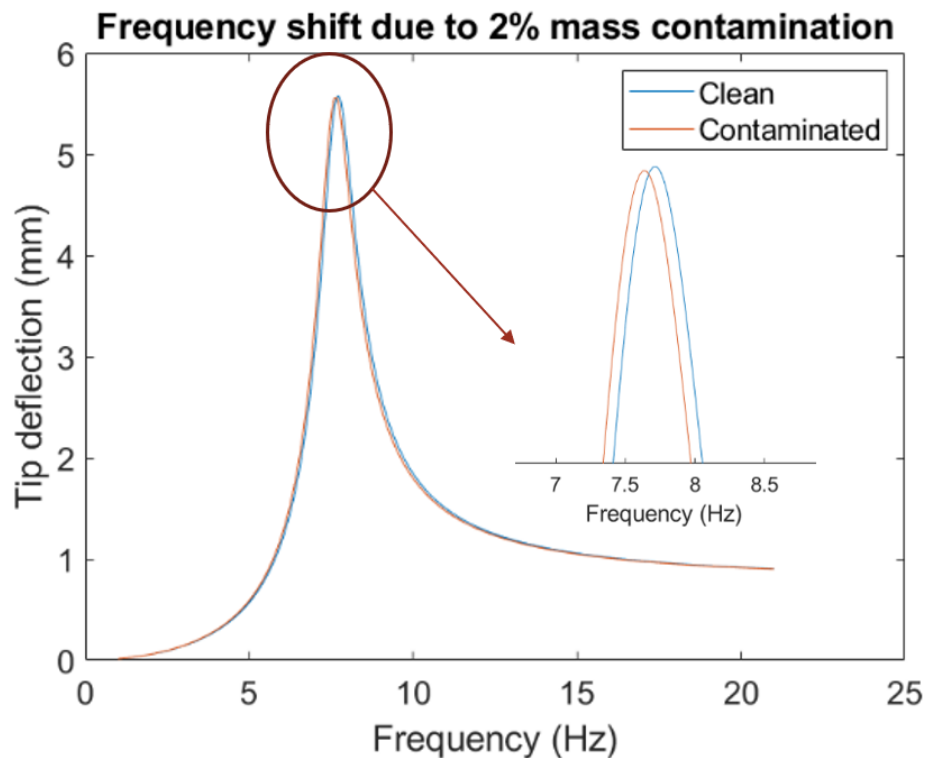| Dimensions	Young's modulus	Poisson's ratio	Mass density	Structural damping ratio
$l \times b \times h$ (mm^3)	E (GPa)	ν	ρ (kg/m^3)	ξ_s
$50 \times 10 \times 0.2$	32	0.33	2710	0.02

Figure 27 Simulated frequency responses of the vibrating beam in water (with and without contaminants).

47

Chapter 6. Conclusion and Future Work

This thesis investigated the applicability of utilizing the ferromagnetic Fe-Cu coating layer on a resonating cantilever beam as a method of real-time sensing of iron contaminations in aqueous solutions for the purpose of monitoring iron levels in drinking water. The experimental results showed the successful synthesis and deposition of the Fe-Cu alloy using the ball milling technique. A linear increase was observed in the produced coating thickness when increasing the milling speed. A similar trend was observed when increasing the milling time. Post magnetization, a 499 nm coating thickness was capable of attracting a maximum value of 7 mg of the iron powder. Moreover, an experimental set-up, made of a mini shaker, a laser distance sensor, and a function generator, was designed, and implemented to test the operability of two different mass sensing mechanisms. It was also used to validate the developed model simulating the vibrations of beams operating in air and water and subject to base excitation. The experimental results showed a good agreement with their counterparts obtained from the model which was also used to investigate the response and limitations of the present sensor.

Finally, to take this work to the next step, the test environment can be taken to a smaller scale with changing the substrate from aluminium to silicon, which is frequently used in MEMS devices and can enhance the magnetic properties of the used material and overcome the issue of lack of surface tension that assists the captured particles stick to the surface. Another approach is replacing the substrate by a mesh-like metal which can be made of green compacted Fe-Cu powder or metal foams, this helps in trapping the captured powder inside the porous. However, other modifications can be investigated on the as-is suggested systems. These include heat treating the coating powder pre-deposition, which can create localized Fe-rich zones leading to an enhancement of the magnetic properties. Moreover, variation in the coating techniques leading to a localized and high-density coating points can strengthen the magnetic field produced by the coating. Furthermore, some modifications to the coating powder, including the FeCoCu alloy can be tested. In addition to optimizing the magnetic behaviour of the coating and further investigating the relation between the coating thickness and the magnetic strength. As for the experimental testing set-up, it can be

further enhanced by deploying a more sophisticated shaker with a frequency resolution below 1 Hz and a transduction mechanism that does not depend on any optical properties for detecting the distance/vibrations. One alternative is to use a capacitive-based transduction technique that requires the use of an underneath electrode and measuring the change in capacitance resulting from the variations in the gap distance separating the vibrating beam from the fixed electrode. Piezoelectric patches made of microfiber composite (MFC) can be also used to detect the small beam deflections from a generated voltage signal.

References

[1] World Health Organization, "Guidelines for drinking-water quality," WHO, Geneva, 2011.

[2] A. Sarkar and S. Shekhar, "Iron contamination in the waters of Upper Yamuna basin," *Groundwater for Sustainable Development,* vol. 7, pp. 421-429, 2018.

[3] P. Patel, N. J. Raju, B. C. S. R. Reddy, U. Suresh, D. B. Sankar and T. V. K. Reddy, "Heavy metal contamination in river water and sediments of the Swarnamukhi River Basin, India: risk assessment and environmental implications," *Environmental Geochemistry and Health,* vol. 40, pp. 609-623, 2018.

[4] R. Thapa, S. Gupta, H. Kaur and S. Rajak, "Search for potential iron contamination zones in Burdwan district: an approach through fuzzy logic," *Sustainable Water Resources Management,* vol. 5, pp. 1017-1031, 2019.

[5] K. K. Borah, B. Bhuyan and H. P. Sarma, "Lead, arsenic, fluoride, and iron contamination of drinking water in the tea garden belt of Darrang district, Assam, India," *Environmental Monitoring and Assessment,* vol. 169, pp. 347-352, 2010.

[6] S. Mirlohi, A. M. Dietrich and S. E. Duncan, "Age-Associated Variation in Sensory Perception of Iron in Drinking Water and the Potential for Overexposure in the Human Population," *Environ. Sci. Technol.,* vol. 45, pp. 6575-6583, 2011.

[7] S. Faham, H. Golmohammadi, R. Ghavami and G. Khayatian, "A nanocellulose-based colorimetric assay kit for smartphone sensing of iron and iron-chelating deferoxamine drug in biofluids," *Analytica Chimica Acta,* vol. 1087, pp. 104-112, 2019.

[8] S. K. Ballas, A. M. Zeidan, V. H. Duong, M. DeVeaux and M. M. Heeney, "The effect of iron chelation therapy on overall survival in sickle," *Am J Hematol,* vol. 93, pp. 943-952, 2018.

[9] R. A. Mandour, "Human health impacts of drinking water (surface and ground) pollution Dakahlyia Governorate, Egypt," *Appl Water Sci ,* vol. 2, pp. 157-163, 2012.

[10] C. P. Wen, J. H. Lee, Y.-P. Tai, C. Wen, S. B. Wu, M. K. Tsai, D. P. Hsieh, H.-C. Chiang, C. A. Hsiung, C. Y. Hsu and X. Wu, "High Serum Iron Is Associated with Increased Cancer Risk," *Cancer Research,* vol. 74, no. 22, pp. 6589-6597, 2014.

[11] K. B. Kim, H. Kim, E. J. Song, S. Kim, I. Noh and C. Kim, "A cap-type Schiff base acting as a fluorescence sensor for zinc(II) and a colorimetric sensor for

iron(II), copper(II), and zinc(II) in aqueous media," *Dalton Transactions,* no. 47, pp. 16569-16577, 2013.

[12] M. Lin, X. Hu, D. Pan and H. Han, "Determination of iron in seawater: From the laboratory to in situ measurements," *Talanta,* vol. 188, pp. 135-144, 2018.

[13] B. Zhang, H. Liu, F. Wu, G. Hao, Y. Chen, C. Tan, Y. Tan and Y. Jiang, "A dual-response quinoline-based fluorescent sensor for the detectionof Copper (II) and Iron(III) ions in aqueous medium," *Sensors and Actuators B: Chemical,* vol. 243, pp. 765-774, 2017.

[14] D. K. Sahu, D. Singha and K. Sahu, "Sensing of iron(III)-biomolecules by surfactant-free fluorescent copper nanoclusters," *Sensing and Bio-Sensing Research,* vol. 22, p. 100250, 2019.

[15] Y.-H. Chan, Y. Jin, C. Wu and D. T. Chiu, "Copper(II) and iron(II) ion sensing with semiconducting polymer dots," *ChemComm,* vol. 47, pp. 2820-2822, 2011.

[16] Z. Li, M. Ti, K. Yanga, X. Li, L. Wu and Y. He, "Colorimetric detection of iron (II) using 4-mercaptobenzoic acid and 3,3′,5,5′-tetramethylbenzidine modified silver nanoparticles," *Microchemical Journal,* vol. 151, p. 104254, 2019.

[17] S. A. Kumar, N. Thakur, H. J. Parab, S. P. Pandey, R. N. Shinde, A. K. Pandey, S. D. Kumar and A. Reddy, "A visual strip sensor for determination of iron," *Analytica Chimica Acta,* vol. 851, pp. 87-94, 2014.

[18] H. R. Mahmoud, M. Saif and R. Fouad, "Novel multi-functional Pr3þ:Bi12SiO20 luminescent nano-sensor for latent human prints, iron ions in drinking water and anticounterfeiting application," *Journal of Alloys and Compounds,* vol. 805, pp. 887-895, 2019.

[19] Q. Zhang, J. Wang, A. M. Kirillov, W. Dou, C. Xu, C. Xu, L. Yang, R. Fang and W. Liu, "Multifunctional Ln–MOF Luminescent Probe for Efficient Sensing of Fe3+, Ce3+, and Acetone," *ACS Appl. Mater. Interfaces,* vol. 10, no. 28, pp. 23976-23986, 2018.

[20] J. Wang, Y. Fan, H.-w. Lee, C. Yi, C. Cheng, X. Zhao and M. Yang, "Ultrasmall Metal–Organic Framework Zn-MOF-74 Nanodots: Size-Controlled Synthesis and Application for Highly Selective Colorimetric Sensing of Iron(III) in Aqueous Solution," *ACS Appl. Nano Mater.,* vol. 1, no. 7, pp. 3747-3753, 2018.

[21] J. Hu, K. Wu, S. Dong and M. Zheng, "A luminescent Cd(II)-MOF as recyclable bi-responsive sensor for detecting TNP and iron(III)/silver(I) with high selectivity and sensitivity," *Polyhedron,* vol. 153, pp. 261-267, 2018.

[22] H. Guo, N. Wu, R. Xue, H. Liu, L. Li, M.-y. Wang, W.-q. Yao, Q. Li and W. Yanga, "Multifunctional Ln-MOF luminescent probe displaying superior

capabilities for highly selective sensing of Fe3+ and Al3+ ions and nitrotoluene," *Colloids and Surfaces A,* vol. 585, p. 124094, 2020.

[23] D. Haldar, P. Duarah and M. K. Purkait, "MOFs for the treatment of arsenic, fluoride and iron contaminated drinking water: A review," *Chemosphere,* vol. 251, p. 126388, 2020.

[24] A. J. Wahl, I. P. Seymour, M. Moore, P. Lovera, A. O'Riordan and J. F. Rohan, "Diffusion profile simulations and enhanced iron sensing in generator-collector mode at interdigitated nanowire electrode arrays," *Electrochimica Acta,* vol. 277, pp. 235-243, 2018.

[25] N. Wang, E. Kanhere, J. Miao and M. S. Triantafyllou, "Miniaturized chemical sensor with bio-inspired micropillar working electrode array for lead detection," *Sensors and Actuators B: Chemical,* vol. 233, pp. 249-256, 2016.

[26] M. Possas-Abreu, F. Ghassemi, L. Rousseau, E. Scorsone, E. Descours and G. Lissorgues, "Development of Diamond and Silicon MEMS Sensor Arrays with Integrated Readout for Vapor Detection," *Sensors,* vol. 17, no. 6, pp. 1163-1178, 2017.

[27] M. A. Saeed, S. M. Khan, N. Ahmed, M. U. Khan and A. Rehman, "Design and analysis of capacitance based Bio-MEMS cantilever sensor for tuberculosis detection," in *International Conference on Intelligent Systems Engineering*, Islamabad, 2016.

[28] N. Jaber, S. Ilyas, O. Shekhah, M. Eddaoudi and M. I. Younis, "Multimode MEMS Resonator for Simultaneous Sensing of Vapor Concentration and Temperature," *IEEE Sensors Journal,* vol. 18, no. 24, pp. 10145 - 10153, 2018.

[29] E. L. Holthoff, L. Li, T. Hiller and K. L. Turner, "A molecularly imprinted polymer (MIP)-coated microbeam MEMS sensor for chemical detection," in *Proc. SPIE 9455, Chemical, Biological, Radiological, Nuclear, and Explosives (CBRNE) Sensing XVI, 94550W*, Baltimore, 2015.

[30] H. J. Pandya, K. Park and J. P. Desai, "Design and fabrication of a flexible MEMS-based electro-mechanical sensor array for breast cancer diagnosis," *Journal of Micromechanics and Microengineering,* vol. 25, no. 7, p. 075025, 2015.

[31] M. Broseghini, L. Gelisio, M. D'Incau, C. A. Ricardo, N. Pugno and P. Scardi, "Modeling of the planetary ball-milling process: The case study of ceramic powders," *Journal of the European Ceramic Society,* vol. 36, pp. 2205-2212, 2016.

[32] C. Suryanarayana, "Mechanical alloying and milling," *Progress in Materials Science,* vol. 46, pp. 1-184, 2001.

[33] L.Takacs and A. Revesz, "Preperation of Coating by Mechanical alloying," *Chemistry for Sustainable Development ,* vol. 15, pp. 231-235, 2007.

[34] X. Huang and T. Mashimo, "Metastable BCC and FCC alloy bulk bodies in Fe–Cu system prepared by mechanical alloying and shock compression," *Journal of Alloys and Compounds,* vol. 288, pp. 299-305, 1999.

[35] A. H. Alami, K. Aokal, A. A. Hawili, R. Hasan and H. Alawadhi, "Facile preparation of graphene coated copper electrodes via centrifugal milling for capacitive deionization applications," *Desalination,* vol. 446, pp. 51-58, 2018.

[36] R. d. O. Hansen, M. Ma´te´fi-Tempfli, R. Safonovs, J. Adam, S. Chemnitz, T. Reimer, B. Wagner, W. Benecke and S. Ma´te´fi-Tempfli, "Magnetic films for electromagnetic actuation in MEMS switches," *Microsyst Technol,* vol. 24, pp. 1987-1994, 2018.

[37] R. Fujiwara, W. Hijikata and T. Shinshi, "Micrometer scale magnetization of neodymium magnet for integrated magnetic MEMS," in *IEEE 29th International Conference on Micro Electro Mechanical Systems (MEMS)*, Shanghai, China, 2016.

[38] J. M. D. Coey, "Magnetism of electrons," in *Magnetism and Magnetic Materials*, Cambridge, Cambridge University Press, 2010, pp. 62-96.

[39] Bleaney, B. I., and B. Bleaney. Electricity and Magnetism, Volume 2, Oxford University Press, Incorporated, 2013.

[40] G. J. Ackland, D. J. Bacon, A. F. Calder and T. Harry, "Computer simulation of point defect properties in dilute Fe—Cu alloy using a many-body interatomic potential," *Philosophical Magazine A,* vol. 75, no. 3, pp. 713-732, 1997.

[41] R. Yavari, O. Drobohlav, A. Hernando, P.Crespo, A. G. Escorial, J. M. Banradiaran and I. Orue, "Metastable Phase Formation and Decomposition in Nanomixtures of Immiscible Cu and Fe," *Materials Science Forum,* vol. 155, pp. 463-474, May 1994.

[42] T.Takeyama, S.Ohnuki and H.Takahashi, "The effect of precipitation on void formation in copper-iron alloy during electron irradiation," *Journal of Nuclear Materials,* vol. 89, no. 2-3, pp. 253-262, 1980.

[43] T. Katayama, Y. Suzuki, H. Awano, Y. Nishihara and N. Koshizuka, "Enhancement of the magneto-optical Kerr rotation in Fe/Cu bilayered films," *Phys. Rev. Lett. ,* vol. 60, no. 14, pp. 1426-1429, 1988.

[44] P. Crespo, A. Hernando, R. Yavari, O. Drbohlav, A. G. Escorial, J. M. Barandiara´n and I. Oru´e, "Magnetic behavior of metastable fcc Fe-Cu after thermal treatments," *Phys. Rev. B,* vol. 48, no. 10, pp. 7134-7139, 1993.

[45] O. Drbohlav and A. R. Yavari, "Magnetic properties of mechanically alloyed nanocrystalline fcc Cu50Fe50 during thermal decomposition," *Journal of Magnetism and Magnetic Materials,* vol. 137, pp. 243-248, 1994.

[46] B. X. Liu, C. H. Shang, L. J. Huang and H.-D. Li, "Fe-Cu icosahedral phase and its thermal and magnetic properties," *Journal of Non-Crystalline Solids,* Vols. 117-118, no. 2, pp. 785-788, 1990.

[47] A. H. Alami, A. A. Hawili and N. Chaker, "Experiments on surface hardening of aluminum components by high-energy centrifugal milling," *The International Journal of Advanced Manufacturing Technology ,* vol. 95, pp. 3855-3862, 2018.

[48] O.Drbohlav and A.R.Yavari, "Mechanical alloying and thermal decomposition of ferromagnetic nanocrystalline f.c.c.-Cu50Fe50," *Acta Metallurgica et Materialia,* vol. 43, no. 5, pp. 1799-1809, 1995.

[49] S. Udara, H. H. C and P. K. Revankar, "Sensitivity and Selectivity Enhancement of MEMS/NEMS Cantilever by Coating of Polyvinylpyrrolidone," *Materials Today: Proceedings,* vol. 18, no. 4, pp. 1610-1619, 2019.

[50] G. Kumar and A. Raman, "Pressure sensor based on MEMS nano-cantilever beam structure as a heterodielectric gate electrode of dopingless TFET," *Superlattices and Microstructures,* vol. 100, pp. 535-547, 2016.

[51] W. J. Choi, Y. Jeon, J.-H. Jeong, R. Sood and S. G. Kim, "Energy harvesting MEMS device based on thin film piezoelectric cantilevers," *Journal of Electroceramics,* vol. 17, pp. 543-548, 2006.

[52] M. Ghommem and A. Abdelkefi, "Nonlinear reduced-order modeling and effectiveness of electrically-actuated microbeams for bio-mass sensing applications," *International Journal of Mechanics and Materials in Design,* vol. 15, pp. 125-143, 2019.

[53] T. Rabenimanana, V. Walter, N. Kacem, P. L. Moal, G. Bourbon and J. Lardiès, "Mass sensor using mode localization in two weakly coupled MEMS cantilevers with different lengths: Design and experimental model validation," *Sensors and Actuators A: Physical,* vol. 295, pp. 643-652, 2019.

[54] R. Bashir, "BioMEMS: state-of-the-art in detection, opportunities and prospects," *Advanced Drug Delivery Reviews,* vol. 56, no. 11, pp. 1565-1586, 2004.

[55] I. Dufour, S. M. Heinrich and F. Josse, "Theoretical Analysis of Strong-Axis Bending Mode Vibrations for Resonant Microcantilever (Bio)Chemical Sensors in Gas or Liquid Phase," *Journal of Microelectromechanical Systems,* vol. 16, no. 1, pp. 44-49, 2007.

[56] A. H. Alami and K. Aokal, "Enhancement of spectral absorption of solar thermal collectors by bulk graphene addition via high-pressure graphite blasting," *Energy Conversion and Management,* vol. 156, pp. 757-764, 2018.

[57] A. H. Alami, K. Aokal, D. Zhang and B. Soudan, "Bulk turbostratic graphene deposition on aluminum substrates via high-pressure graphite blasting," *Applied Nanoscience,* vol. 8, pp. 1943-1950, 2018.

[58] A. H. Alami, J. Abed, M. Almheiri and A. Alketbi, "The Fe-Cu Metastable Nano-scale Compound for Enhanced Absorption in the UV–Vis and NIR Ranges," *Metallurgical And Materials Transactions E,* vol. 2, pp. 229-235, 2015.

[59] Y. Aboelkassem, A. H. Nayfeh and M. Ghommem, "Bio-mass sensor using an electrostatically actuated microcantilever in a vacuum microchannel," *Microsystem Technologies,* vol. 16, p. 1749–1755, 2010.

Appendix

In this Appendix the Mathematica Code used to produce the numerical results of this study is presented.

```mathematica
In[1]:= NumRul = {E0 → 32 × 10^9, ν → 0.33, ρ → 2710, h → 0.2 × 10^-3, b → 10 × 10^-3,
          L → 50 × 10^-3, λ₀ → 1.875104, ρf → 1000, μ → 0.001}; (* System parameters *)

In[2]:= D0 = E0 (b h³/12) /. NumRul;  (* Flexural rigidity *)

In[3]:= ms = ρ b h /. NumRul ; (* mass of the beam per unit length *)

In[4]:= Ac = 0.00;
        (* total mass of the coating and any
           absorbed iron as fraction of the mass of the beam *)

In[5]:= Ac * ρ b h L * 1000000 /. NumRul;

In[6]:= ParaRul =
          {MLL → π ρf b²/4, a₁ → 1.0553, a₂ → 3.7997, bb₁ → 3.8018, bb₂ → 2.7364} /. NumRul // Flatten //
          N;

In[7]:= fvacuum = λ₀²/(2 π L²) √(D0/(ρ b h (1 + Ac))) /. NumRul ;

        (* first natural frequency (beam + coating) in vacuum in Hz *)

In[8]:= g₂ = MLL (a₁ + a₂ √(2 μ/(ρf 2 π f₀ b²))) /. ParaRul /. NumRul;

        fRule = FindRoot[f₀ - fvacuum/√(1 + g₂/(ρ b h)) /. ParaRul /. NumRul, {f₀, fvacuum}] ;

In[10]:= Am = 2 * g₂/(ρ b h) /. fRule /. ParaRul /. NumRul ; (* added mass coefficient *)

        g₁ = MLL 2 π f₀ (bb₁ √(2 μ/(ρf 2 π f₀ b²)) + bb₂ 2 μ/(ρf 2 π f₀ b²)) /. fRule /. NumRul;

        ζh = g₁/(4 π fvacuum ρ b h √(1 + g₂/(ρ b h))) /. fRule /. ParaRul /. NumRul ;

In[12]:= fvacuum/√(1 + Am) /. fRule ; (* first natural frequency in water *)

In[13]:= m = ms (1 + Am + Ac) /. NumRul ; (* total mass per unit length *)

In[14]:= φ[x] = √(1/(m L)) (Cosh[λ₀ x/L] - Cos[λ₀ x/L] - 0.734095 (Sinh[λ₀ x/L] - Sin[λ₀ x/L])) /. NumRul ;
        (* mass normalized mode shape *)

In[15]:= φL = φ[x] /. x → L /. NumRul;

In[16]:= θ = m ∫₀^L φ[x] dx /. NumRul;

In[17]:= ωwater = 2 * π * fvacuum/√(1 + Am) /. fRule;
```

```
In[18]:= ζs = 0.0425; (* to be determined experimentally *)
```

```
In[19]:= ζ = ζh + ζs;
```

```
In[20]:= Y = 0.0005; (* amplitude of base excitation in m *)
```
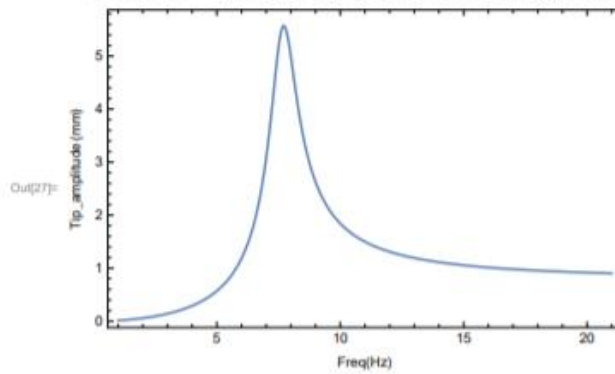
```
In[21]:= It = 0;
        ListW = {};
        ListMatf = {};
        ListMatW = {};
        Δ = 0.05;
```

```
In[26]:= While[It ≤ 400,   (* number of steps *)
         Ω = (1 + Δ * It) * 2 * π;
         W = Abs[ (Y θ Ω² φL) / (ωwater² - Ω² + 2 i ζ ωwater Ω) ] * 1000;
         ListW = Insert[ListW, {Ω / (2 * π), W}, -1];
         It++;
         ListMatf = Join[ListMatf, {Ω / (2 * π)}];
         ListMatW = Join[ListMatW, {W}];
        ]
```

```
In[27]:= ListPlot[ListW, Frame → True,
         FrameLabel → {Freq [Hz], Tip_amplitude[mm]}, Joined → True, PlotRange → All]
```

Vita

Abdullah was born in 1994, in Fujairah, United Arab Emirates. He received his primary and secondary education in Fujairah, UAE. He received his B.Sc. degree in Mechanical Engineering from the University of Sharjah in 2018.

In September 2018, he joined the Mechanical Engineering master's program in the American University of Sharjah as a graduate teaching assistant. His research interests are in Mechanical alloying and Materials Engineering and Manufacturing.